Topical Review

Superconducting RF materials other than bulk niobium: a review

Anne-Marie Valente-Feliciano

Thomas Jefferson National Accelerator Facility, Newport News VA, USA

E-mail: valente@jlab.org

Abstract

For the past five decades, bulk niobium (Nb) has been the material of choice for superconducting RF (SRF) cavity applications. Alternatives such as Nb thin films and other higher-T_c materials, mainly Nb compounds and A15 compounds, have been investigated with moderate effort in the past. In recent years, RF cavity performance has approached the theoretical limit for bulk Nb. For further improvement of RF cavity performance for future accelerator projects, research interest is renewed towards alternatives to bulk Nb. Institutions around the world are now investing renewed efforts in the investigation of Nb thin films and superconductors with higher transition temperature T_c for application to SRF cavities. This paper gives an overview of the results obtained so far and challenges encountered for Nb films as well as other materials, such as Nb compounds, A15 compounds, MgB_2, and oxypnictides, for SRF cavity applications. An interesting alternative using a superconductor–insulator–superconductor multilayer approach has been recently proposed to delay the vortex penetration in Nb surfaces. This could potentially lead to further improvement in RF cavities performance using the benefit of the higher critical field H_c of higher-T_c superconductors without being limited with their lower H_{c1}.

Keywords: superconductor, RF cavities, superconductivity, materials

1. Introduction

For the past five decades, bulk niobium (Nb) has been the material of choice for superconducting RF (SRF) applications such as accelerating cavities for particle accelerators. The primary reason is that Nb has the highest critical temperature ($T_c = 9.25\ K$) and the highest lower magnetic field H_{c1} of all the pure metals. In addition, it is relatively simple to use in terms of fabrication. Many compounds (including the new high-T_c ceramic materials) have shown higher critical temperatures than Nb. However, at present, none of these materials can match Nb in terms of its performance with increasing RF fields or its ease of use for accelerator applications. The RF performance of bulk Nb cavities has continuously improved over the years and is approaching the intrinsic limit of the material ($H \sim H_c \sim 200$ mT) [1]. Although some margin seems still available with processes such as N surface doping [2–4], long term solutions for SRF surface efficiency enhancement need yet to be pursued. Achieving the magnetic field limitation means that no further increase in the accelerating electrical field of bulk Nb cavities can be expected. For further improvement in cavity RF performance, innovation is needed and one may have to turn to other forms of Nb and to other superconducting materials. The potential benefits of using other materials than Nb would be a higher T_c, a potentially higher critical field H_c, leading to potentially significant cryogenics cost reduction if the cavity operation temperature is 4.2 K or higher. If the thin film route is chosen, the use of substrates with higher thermal conductivity could also lead to substantial cost reduction in cryomodules

fabrication (for example, easily castable aluminum (Al) or copper (Cu), reduction in microphonics…).

2. Criteria for materials suitable to SRF applications

For a superconducting material to be a good candidate for SRF applications, a high critical temperature is not sufficient. A comprehensive review of the different classes of superconductors for cavity applications has been given by Palmieri [5] a few years ago.

2.1. Surface resistance

Although superconductors do not exhibit any dc resistivity, there are small losses for RF currents, which can be explained by a model of inter-penetrating normal conducting electrons and superconducting Cooper pairs when $T > 0$ (two-fluid model [6]). Collisions between Cooper pairs and lattice defects, impurities or phonons are insufficient to split the pairs and scatter them out of the ground state. Any current carried by these pairs flows without resistance. However, unpaired electrons can be scattered and dissipate energy. However, the lossless Cooper pairs current expel any fields in the superconductor so the dc resistivity of a superconductor is zero. In this case, the normal conducting electrons do not see an electric field and do not contribute to the current flow.

In the RF case, although Cooper pairs cannot be scattered, they do possess inertia. At microwave frequencies, they no longer screen completely externally applied fields and normal conducting electrons are then accelerated, causing power dissipation. The surface resistance of the superconductor decreases as the number of unpaired electrons declines exponentially with temperature.

The application of the two fluid model yields a surface resistance R_s that drops exponentially to zero at $T = 0$:

$$R_s \propto \omega^2 e^{\left(-\frac{\Delta(T)}{k_B T}\right)}, \qquad \left(T \leqslant \frac{T_c}{2}\right). \tag{1}$$

In practice, as shown in figure 1, the surface resistance never vanishes due to the presence of a temperature independent residual term of several nΩ [7]:

$$R_s = R_{BCS}(T) + R_{res}. \tag{2}$$

BCS resistance. With T the working temperature and T_c the superconducting transition temperature, the surface resistance can be expressed [8] using the following approximated formula (for $T \leqslant T_c/2$):

$$\frac{R_s}{R_n} = \frac{1}{\sqrt{2}} \frac{\frac{\sigma_1}{\sigma_n}}{\left(\frac{\sigma_2}{\sigma_n}\right)^{\frac{3}{2}}}. \tag{3}$$

For $\hbar\omega < 2\Delta$, σ_1/σ_n and σ_2/σ_n are two integral relations for the complex conductivity of a superconductor found in the framework of the BCS theory extension to finite frequencies [9].

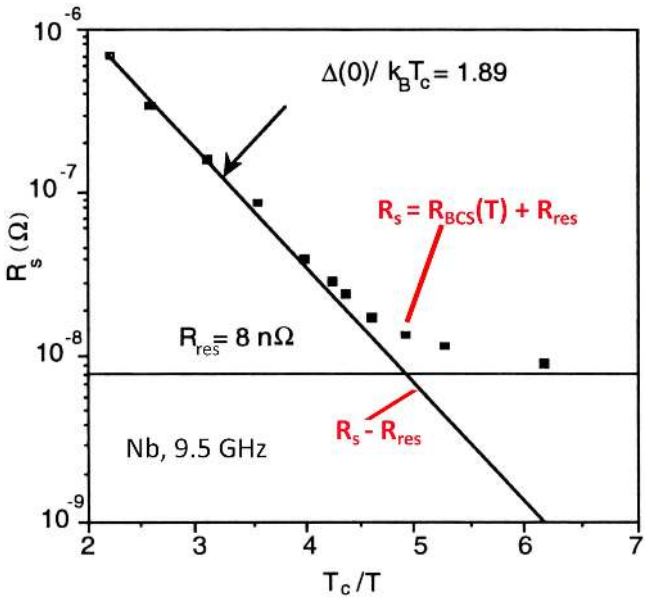

Figure 1. Surface resistance for Nb at 9.5 GHz with a residual resistance $R_{res} = 8$ nΩ and $\Delta(0)/k_B T_c = 1.89$.

$$\frac{\sigma_1}{\sigma_n} = \frac{2}{\hbar\omega} \int_{\Delta}^{\infty} [f(E) + f(E + \hbar\omega)] g^+(E) dE \tag{4}$$

$$\frac{\sigma_2}{\sigma_n} = \frac{1}{\hbar\omega} \int_{\Delta - \hbar\omega, -\Delta}^{\infty} [1 - 2f(E + \hbar\omega)] g^-(E) dE, \tag{5}$$

where

$$\begin{aligned} f(E) &= \frac{1}{1 + \exp\left(\frac{E}{k_B T}\right)} \\ g^{\pm} &= \frac{E^2 + \Delta^2 + \bar{h}\omega E}{\sqrt{\pm(E^2 - \Delta^2)(E + \bar{h}\omega)^2 - \Delta^2}}. \end{aligned} \tag{6}$$

The analytical approximation in the normal skin effect regime (for $\bar{h}\omega < 2\Delta$) of these integrals leads to the following formula for R_{BCS} (valid in the dirty limit and for $T \leqslant T_c/2$)

$$\begin{aligned} R_{BCS} &= \frac{R_n}{\sqrt{2}} \left(\frac{\hbar\omega}{\pi\Delta}\right)^{\frac{3}{2}} \frac{\sigma_1}{\sigma_n} \\ &= A\sqrt{\rho_n} \frac{e^{\frac{-\Delta}{k_B T}}}{\sqrt{s T_c} T \left(1 + e^{\frac{-\Delta}{k_B T}}\right)^2} \omega^2 \ln \frac{\Delta}{\hbar\omega}, \end{aligned} \tag{7}$$

where A is a constant weakly dependent on the material, ω is the RF frequency, ρ_n is the normal state resistivity, λ is the penetration depth and T_c the transition temperature.

In this expression, the dependence of R_{BCS} on ρ_n and T_c represents an immediate criterion for selecting potential candidate materials for SRF cavity applications. Although equation (7) is approximated and limited to dirty superconductors, it clearly shows how low R_{BCS} values can be obtained by reducing ρ_n and increasing T_c. The BCS theory predicts then that a good candidate for RF applications must be a high T_c material but also a good metal in the normal state (low ρ_n).

Residual losses. The surface resistance residual term, $R_{\rm res}$, is temperature independent and attributed to parasitic losses. To this day, it is not fully understood. Many reports exist in the literature about the possible origin of the residual resistance: both *intrinsic losses*(such as non-ideal surface quality, metallic inclusions within the penetration depth, surface oxides, and grain boundaries) and *accidental mechanisms* (such as particulates, chemical residues or surface defects on the cavity walls) contribute to parasitic losses. Other contributors are extrinsic losses due to flux trapped during cooling. Due to the wide variety of phenomena at play, the prediction of these residual losses with one formula is impossible. However, from results reported in literature, $R_{\rm res}$ is found empirically to be at least proportional to $\sqrt{\rho_{\rm n}}$. Therefore, among two different materials with different ρ_n and $T_{\rm c}$ values, having the same $R_{\rm BCS}$, the one with the lower $\rho_{\rm n}$ should have the smallest residual resistance.

2.2. Critical magnetic fields

When electrons condense into Cooper pairs, the resulting superconducting state becomes more highly ordered than the normal-conducting state. Since only those few electrons within $k_B T_{\rm c}$ of the Fermi energy are involved, the entropy difference is small. The free energy in the superconducting state is lower than that in the normal-conducting one. Here free energy is

$$F = U_{\rm int}(T) - TS, \tag{8}$$

where $U_{\rm int}$ is the internal energy and S the entropy. As mentioned earlier, when an external dc magnetic field $H_{\rm ext}$ is turned on, supercurrents flow in the penetration depth to cancel out the field in the interior. This raises the free energy of the superconducting state

$$F_{\rm s}(H) = F_{\rm n} = F_{\rm s}(H=0) + \mu_0 V_{\rm s}\int_0^{H_{\rm c}} H{\rm d}H \tag{9}$$

Here $V_{\rm s}$ is the superconductor volume. All the flux enters the superconductor at $H_{\rm c}$, which is the thermodynamic critical field. The second term in equation (9) is the work done on the superconductor to establish the screening currents:

$$F_{\rm n} - F_{\rm s}(H) = \frac{\mu_0 V_{\rm s} H_{\rm c}^2}{2}. \tag{10}$$

The BCS theory leads to an expression for the free energy of electrons in the superconducting state from which various thermodynamic properties, including $H_{\rm c}$, can be derived.

In particular, one can calculate the zero temperature thermodynamic critical field $H_{\rm c}$:

$$\frac{\mu_0 H_{\rm c}^2}{2} = \frac{3\gamma T_{\rm c}^2}{4\pi^2}\left(\frac{\Delta(0)}{k_B T_{\rm c}}\right)^2 = 0236\gamma T_{\rm c}^2. \tag{11}$$

Here γ is the coefficient of the linear electronic specific heat in the normal state ($(\pi 2/3)k_B^2 g(\epsilon_F)$). It is important to note that the thermodynamic critical field increases proportionally to $T_{\rm c}$. Therefore, the higher transition temperature superconductors, such as Nb_3Sn, are interesting for accelerating cavities because of the promise of higher operating fields. Note that γ is related to the electronic density of states and thereby reflects the role of the electronic structure of the material.

The elementary BCS prediction for $H_{\rm c}(T)$ is often expressed by the empirical law:

$$\frac{H_{\rm c}(T)}{H_{\rm c}(0)} = 1 - \left(\frac{T}{T_{\rm c}}\right)^2. \tag{12}$$

Type I-superconductors remain in the Meissner state until the critical field $H_{\rm c}$ is reached which forces the material into the normal state.

Type II-superconductors have three phases: the Meissner, mixed and normal states. They are then characterized by two critical fields:

- The lower critical field $H_{\rm c1}$ at which the material transitions from a complete Meissner state to the mixed state where flux penetration starts. The material becomes finely divided in normal and superconductive domains in periodic arrangements (flux vortices).
- The upper critical field $H_{\rm c2}$ above which the material becomes fully normal.

The generalized magnetic response of both classes of superconductors is represented in figure 2.

Nb is a marginal type II-superconductor for which its critical fields are very close in value. At zero temperature, ${H_{\rm c1}}^{\rm Nb} = 170\,{\rm mT}$, ${H_{\rm c}}^{\rm Nb} = 200\,{\rm mT}$, ${H_{\rm c2}}^{\rm Nb} = 240\,{\rm mT}$.

Superheating field. In the presence of an external magnetic field, the superconductor to normal-conductor transition is of first order at $T = T_{\rm c}(H)$, and is combined with a latent heat due to the entropy discontinuity. The first order phase transition takes place at nucleation centers. Because of the entropy discontinuity and nucleation centers, a *superheated* superconducting state can persist metastably at $H > H_{\rm c}$.

In a type I superconductor, the positive surface energy suggests that, in dc fields, the Meissner state could persist beyond the thermodynamic critical field, up to the superheating field $H_{\rm sh}$. At this field, the surface energy per unit area vanishes (figure 2):

$$\frac{\mu_0}{2}H_{\rm c}^2\xi - H_{\rm sh}^2\lambda = 0,\ H_{\rm sh} = \frac{1}{\sqrt{\kappa_{\rm GL}}}H_{\rm c}. \tag{13}$$

For type II superconductors, it is also possible for the Meissner state to persist metastably above the lower critical field $H_{\rm c1}$.

The dependence of the superheating field, $H_{\rm sh}$, on the GL parameter $\kappa_{\rm GL}$ and the thermodynamic critical field, $H_{\rm c}$, has been calculated by solving the GL equations [12] leading to:

$$H_{\rm sh} \approx \frac{0.89}{\sqrt{\kappa_{\rm GL}}}H_{\rm c} \qquad \kappa \ll 1, \tag{14}$$

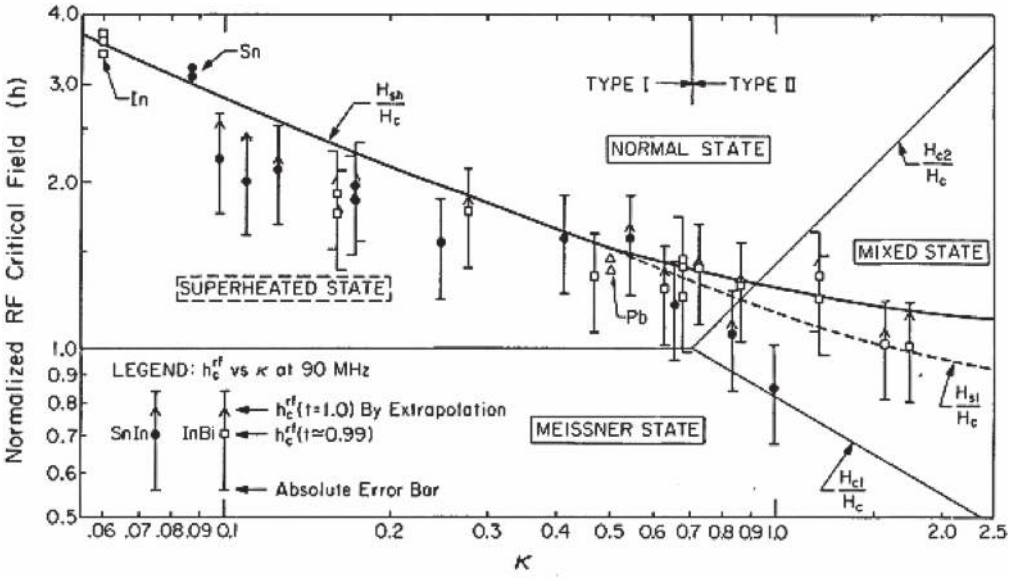

Figure 2. Normalized critical field as a function of the GL parameter $\kappa_{GL} = \frac{\lambda}{\xi}$, from [10], copyright 1977 The American Physical Society.

$$H_{sh} \approx 1.2H_c \qquad \kappa \approx 1, \tag{15}$$

$$H_{sh} \approx 0.75H_c \qquad \kappa \gg 1. \tag{16}$$

High magnetic fields are present in SRF cavities, with, in many cases, an amplitude approaching the order of magnitude of the superconducting material critical magnetic fields. Since the nucleation time of a vortex is usually large compared to the RF period and because it is theoretically possible to maintain a metastable Meissner state up to H_{sh}, the critical RF field H_c^{RF} is estimated to be equal to H_{sh} [7] as suggested by some experiments conducted in the pulsed regime [10, 11]. For type II superconductors, H_{sh} can be significantly larger than H_{c1}.

2.3. Superconducting gap symmetry

The high Q required for SRF cavities results from a minimal surface resistance which is dependent on the superconducting gap Δ (equation (7)). All conventional BCS superconductors have an s-wave gap symmetry. Many high-T_c superconductors (HTS) such as cuprates are d-wave superconductors with nodes in the gap. At low temperatures, d-wave cuprates or heavy fermions cannot compete with s-wave low-T_c materials.

In summary, the criteria for a superconducting material to be a good candidate for SRF application are:

- A large superconducting gap Δ, thus a high T_c.
- No node in the gap symmetry.
- A metallic behavior i.e. a low normal resistivity ρ_n.
- A high H_c or H_{sh} and a small GL parameter κ.
- Finally, the material and format chosen needs to be able to sustain fabrication and surface preparation processes.

3. Candidate alternative materials to bulk Nb

In view of the criteria cited in the previous section, the choice of bulk Nb for SRF applications was natural. It has the highest T_c and H_{c1}, H_{sh} of all pure metals. Also, as a marginal type II superconductor, it is the best compromise for the requirements mentioned previously. However, SRF cavities using bulk Nb are reaching RF performances approaching its theoretical limit ($H \sim H_c\,(0) \sim 200$ mT) [1].

Achieving the magnetic field limitation means that no further increase in the accelerating electrical field of bulk Nb cavities can be expected. For further improvement of cavities' RF field performance, innovation is needed and one may have to turn to other superconducting materials. Several avenues can be considered.

3.1. Nb thin films

Due to the very shallow penetration depth of RF fields (only ~40 nm for Nb), SRF properties are inherently a surface phenomenon, involving a material thickness of less than 1 μm. Instead of using bulk Nb, one can then foresee the merits of depositing a Nb film on the inner surface of a castable cavity structure made of copper (Cu) or aluminum (Al). At the system design level, this would allow one to decouple the active SRF surface from the accelerating structure definition and its cooling, bringing dramatic change to the cost framework of SRF accelerators.

3.2. Other superconducting materials

The realm of superconducting compounds (see figure 3) has been much less explored in the past for SRF properties because of the technical complexities that govern compound formation. In evaluating candidates, it is important to select a material for which the desired compound phase is stable over

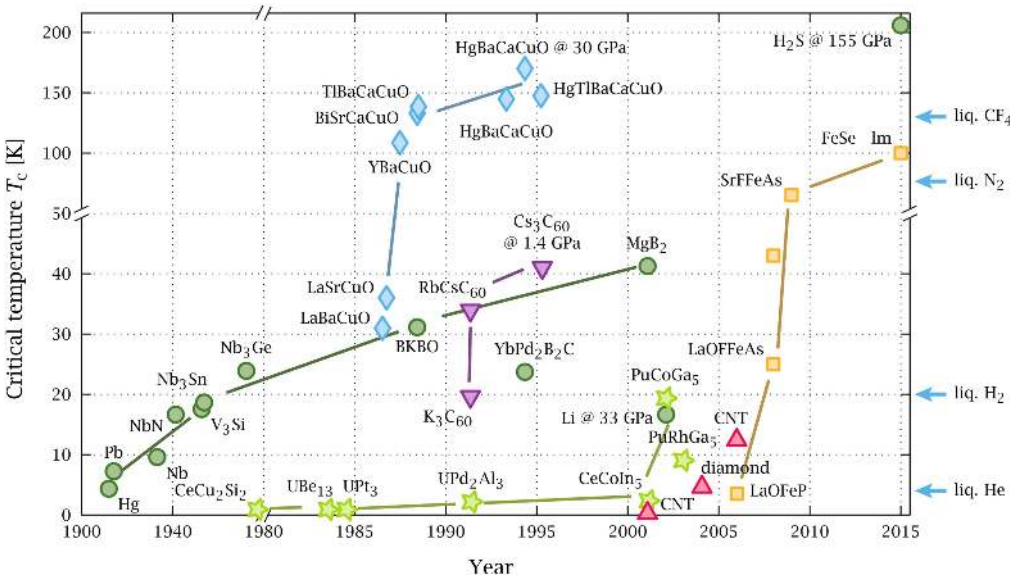

Figure 3. Superconductors transition temperature T_c versus their year of discovery [13] courtesy of P J Ray.

Table 1. Superconducting parameters for some candidate materials considered for SRF applications.

Material	T_c (K)	ρ_n ($\mu\Omega$ cm)	$H_c(0)$ (T)	$H_{c1}(0)$ (T)	$H_{c2}(0)$ (T)	λ (nm)	Δ (meV)	ξ (nm)
Nb	9.23	2	0.2	0.18	0.28	40	1.5	35
NbN	16.2	70	0.23	0.02	15	200–350	2.6	3–5
NbTiN	17.3	35		0.03	15	150–200	2.8	5
Nb_3Sn	18	8–20	0.54	0.05	28	80–100	3.1	4
V_3Si	17	4	0.72	0.072	24.5	179	2.5	3.5
Nb_3Al	18.7	54			33	210	3	
Mo_3Re	15	10–30	0.43	0.03	3.5	140		
MgB_2	40	0.1–10	0.43	0.03	3.5–60	140	2.3 /7.2	5
Pnictides	30–55		0.5–0.9	30	50–135	200	10–20	2

a broad composition range. For further improvement of RF cavity performance for future accelerator projects, research interest is renewed towards alternative materials to Nb.

As mentionned above, good candidate superconductors for SRF applications need to have a high T_c and low resistivity in the normal state to minimize RF losses. To maximize accelerating gradients, a high H_c or H_{sh} and small κ are necessary. Among the thousands of known conventional superconductors, only a limited number of compounds have a critical temperature higher than Nb and present a potential as candidate materials for SRF cavity applications (see table 1).

3.3. High-T_c material based multilayer structures

In 2006, a concept was proposed by Gurevich [1] which would allow one to take advantage of HTSs without being penalized by their lower H_{c1}. The idea is to coat SRF cavities with alternating superconducting and insulating layers (superconductor–insulator–superconductor (SIS) structures) with a thickness smaller than the penetration depth λ. If the superconducting film is deposited with a thickness $d \ll \lambda$, the Meissner state can be retained at magnetic field much higher than bulk H_{c1}. The higher-T_c thin layers provide then magnetic screening of the bulk superconducting cavity without vortex penetration. The strong increase of first flux entry magnetic field H_{fp} in films allows to use RF fields higher than the critical field H_c of Nb, but lower than those at which the flux penetration at grain boundaries may create a problem. The BCS resistance is also strongly reduced with the use of superconducting layers with higher gap Δ (Nb_3Sn, NbTiN, …). With such structures, Q-values at 4.2 K of two orders of magnitude above Nb values could be achieved. As an example, a thin Nb_3Sn film of 20 nm in thickness increases the flux entry magnetic field H_{fp} for Nb_3Sn to 5.7 T. If a 50 nm Nb_3Sn layer is coated on a bulk Nb cavity with an insulator layer in between, and if the Nb cavity can sustain fields up to 150 mT, this structure is predicted to sustain external magnetic field of about 320 mT and therefore could support accelerating gradient without precedent. Several laboratories around the world have started to investigate this idea. The influence of the morphology and composition of grains, the influence of the materials composition on H_{fp}, H_{c1}, and H_c have to be evaluated. A certain number of technical challenges will have to be surmounted for practical application to SRF cavities, but a successful implementation would

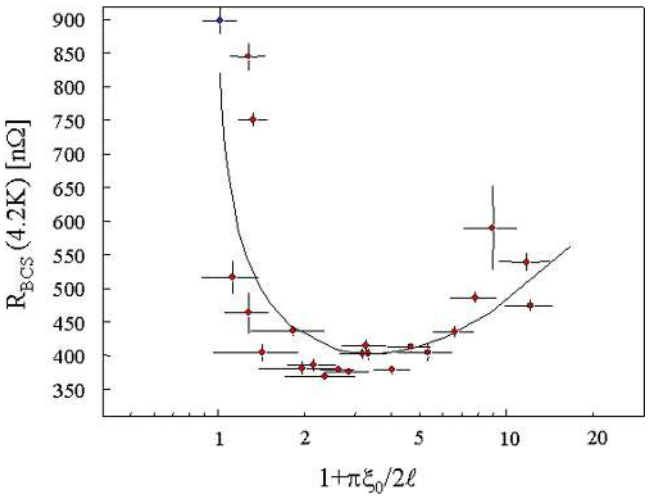

Figure 4. The BCS surface resistance at 1.5 GHz as a function of Nb purity. The abscissa is equal to 1 in the limit of electron mean free path $l \rightarrow \infty$ (from [14], copyright 1999 Elsevier).

lead to higher accelerating gradients and potentially significant cryogenics cost reduction if the cavity operation temperature is 4.2 K or higher.

4. Nb thin films

Superconducting Nb/Cu cavities produced by the magnetron sputtering technology have been successfully exploited at CERN with LEP-II II (352 MHz, 4 K) and LHC (400 MHz, 4 K). This technology is also employed in several other present or future accelerator facilities, such as ALPI (INFN-LNL) or HIE-ISOLDE (CERN). Nb films show clear advantage compared to bulk Nb for defined accelerator parameter sets, in particular for low cavity frequencies or for operation at 4.2 K. The BCS surface resistance for thin films is lower than for bulk Nb, due to a normal state electrical resistivity close to the theoretical optimum (see figure 4).

4.1. Motivation for Nb thin film technology for SRF applications

Thermal stability. High purity bulk Nb has a typical heat conductance of about 75 $W\,m^{-1}$ at 4.2 K, while Cu heat conductance is as high as 300–2000 $W\,m^{-1}$. Thus the amount of heat generated by a defect inside a superconducting cavity (typically 10 mW for a 40 mT RF magnetic field in the area of a 50 μm size defect) can be more easily conducted to the helium bath in the case of a Cu cavity substrate. A thermal breakdown model for defects in a resonant cavity [15] allows simulations which accurately illustrate the effect of the defect size and the Nb purity level (represented by RRR, residual resistivity ratio). The large thermal conductivity of Cu helps the thin film cavity to be more resis to multipacting and field emission.

Low cost. The cost of Cu material is only about 10% of the cost of bulk Nb. This is especially advantageous for accelerators operating at low frequencies since the dimensions of the cavities are inversely proportional to their operating frequency. The cavity manufacturing cost associated with Cu can also be substantially lower than with bulk Nb. Decoupling the SRF surface (Nb film) from its substrate can also open the way to significant simplifications in cryomodule design, thus affecting the building cost.

Insensitivity to Earth magnetic field trapping. One source of residual resistance in the Nb surface is trapped magnetic flux. Nb films have shown an unexpected advantage, in that their surface resistance is almost insensitive to the Earth's magnetic field, eliminating the need of complex cavity magnetic shielding [7, 16]. The effect of the Earth's magnetic field is 100 $n\Omega\,Gs^{-1}$ of external magnetic field for bulk Nb, and only 1 $n\Omega\,Gs^{-1}$ for Nb films.

Freedom from undissolved inclusions. Due to the manufacturing process (pressing, rolling and melting, etc), the Nb sheet or the Cu sheet typically present micro-inclusions, typically elements such as steel, nickel and some oxide compounds. Though not necessarily a cause of decrease of the metal sheet RRR, they can be distributed deep inside the material and can be uncovered with etching. Such inclusions are caused during the cooling process by precipitation of some compound dissolved in the molten Nb and present in amounts exceeding the solubility. Although these inclusions' content can be well controlled, the resulting added process steps do increase the cost for raw bulk material as well as the cost for extra processing during cavity manufacturing. Additionally, inclusions are very easily introduced into bulk Nb from machining tools [17]. In general, vacuum deposition of thin film is Known to produce excellent surface quality in many applications.

4.2. State of the art for SRF Nb films

4.2.1. Elliptical Nb/Cu cavities: the CERN LEP-II and LHC experience and R&D on 1.5 GHz Nb/Cu magnetron sputtered cavities. CERN has conducted pioneering studies [18–20] in the field of SRF Nb/Cu films applied to cavities and successfully implemented this technology in LEP-II [15] and LHC accelerators [20].

In operation from 1989 to 2000, the LEP-II machine was composed of 288 cavities (4-cells, 352 MHz). The cavities were prepared by cylindrical magnetron sputtering. Their performance is shown in figure 5(a). The current LHC machine relies on 16 low impedance 400 MHz Nb/Cu single cell cavities [20] that were produced in industry. The same technology was applied for the coatings while integrating the lessons learned over the years from bulk Nb cavity processing. The LHC cavity specifications are $Q = 2 \times 10^9$ at $E_{acc} = 5.5\,MV\,m^{-1}$ and 4.5 K. The LHC cavities exhibit good Q versus E_{acc} performance (figure 5(b)) [21].

Once LEP-II was in operation, R&D efforts concentrated in material and superconducting studies aiming at determining the ultimate performance for sputtered Nb/Cu cavities. The work was conducted on small samples and 1.5 GHz cavities. Although 1.5 GHz cavities achieving gradients up around 25 $MV\,m^{-1}$ [22] were commonly produced, these cavities suffered from significant losses resulting in the reduction of Q at accelerating gradients above 15 $MV\,m^{-1}$

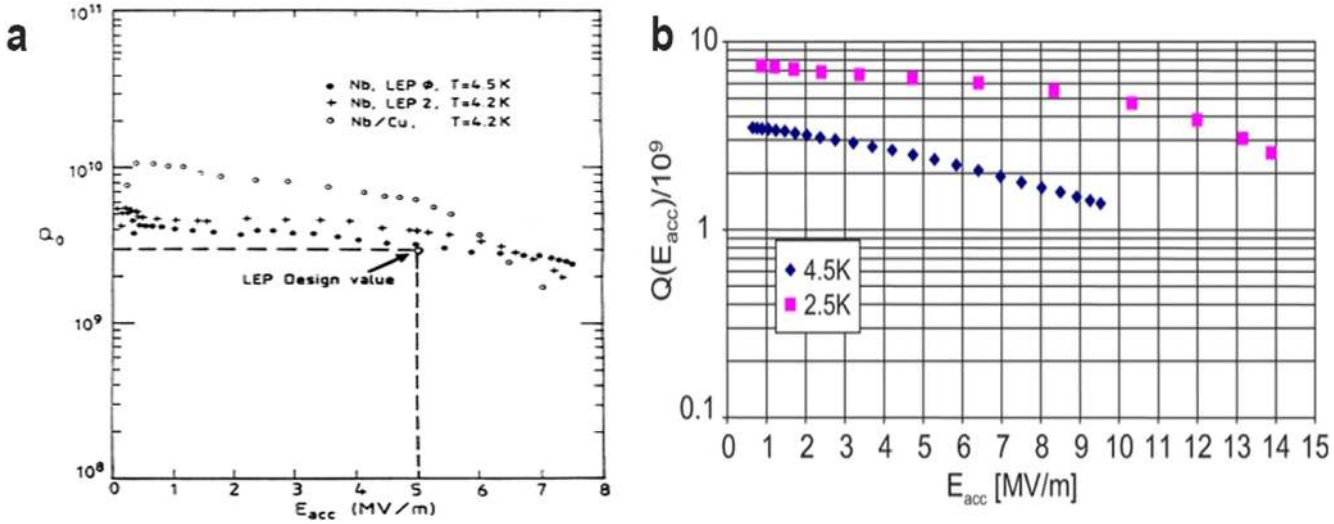

Figure 5. RF performance for LEP-II prototypes from [15] (a) and typical industry-produced LHC 400 MHz cavity RF performance from [20], copyright 2006 Elsevier (b).

(figure 6). Some of the defects were most likely inherent to the magnetron sputtering technique used to produce these cavities.

One interesting note is that all of these cavities exhibit, at low temperature, an increase in Q at the 10^{11} level and beyond at very low accelerating field (figure 6) and one cannot help but compare this behavior to the one recently observed for N or Ti doped bulk Nb cavities [3, 4] and the prediction from Xiao's extended BCS theory as reported in [23].

4.2.2. Dc bias diode sputtered Nb/Cu quarter-wave resonators (QWR). The Nb/Cu technology was also implemented for more complicated cavity structures such as QWR (figure 7(a)). ALPI is a superconducting linac for heavy ions, in operation at INFN-LNL (Italy) since 1994 [24]. Originally the sputtered medium β cavities installed in ALPI were Pb plated. Since the very beginning of the ALPI project two R&D programs were launched in parallel, one on the sputtering of Cu bases with Nb and the other on the realization of bulk Nb cavities [25]. These programs brought ALPI to the outstanding result of an accelerating field of more than 6 MV m^{-1} in 1993.

In view of the R&D program success, Nb/Cu technology was adopted for the higher β section in ALPI second phase. By implementing new design details, along with a careful and long setup of the sputtering procedure, the first results were confirmed and often exceeded with an average accelerating field $E_{acc} >$ 6–8 MV m^{-1} at $P_{dissipated} = 7$ W (with $Q_0 > 6 - 7 \times 10^8$ at the high field values). 52 quarter wave Nb/Cu resonators [25]) are now installed. The success of the higher β cavities based on Nb/Cu technology led to the refurbishment of the medium β section of the linac By replacing the original Pb layer with a sputtered Nb film, the accelerating field of these cavities exceeds 4 MV m^{-1} at 7 W dissipated power.

More recently, the new HIE-ISOLDE accelerator at CERN requires the production of 32 superconducting quarter-wave cavities (20 high-β and 12 low-β) in order to increase the energy of the rare isotope beam delivered to the experiments [26, 27]. In view of the success of the ALPI accelerator, dc bias diode sputtering has been chosen to prepare these cavities. Figures 7(b) and (c) show the RF performance for some HIE-ISOLDE cavity prototypes along with the microstructure of the Nb film.

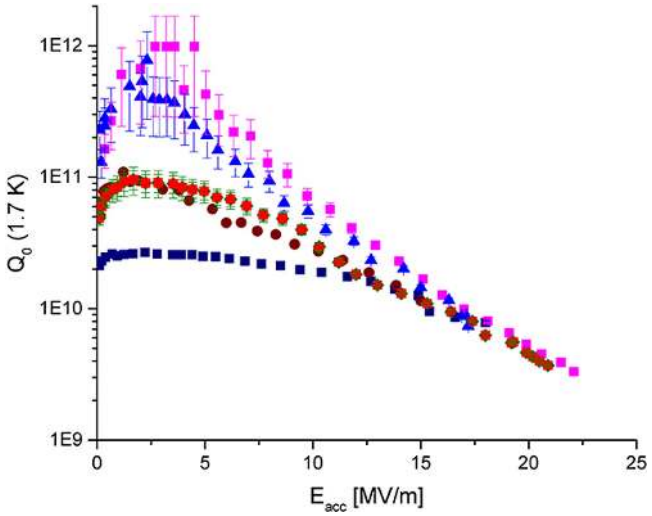

Figure 6. Best RF performance at 1.7 K for several 1.5 GHz Nb/Cu cavities sputtered coated with Kr at CERN [22]. The symbols correspond to individual Nb films.

4.2.3. Characteristics of sputtered Nb/Cu films

Non-quadratic RF losses. The BCS component of the surface resistance reduces exponentially with temperature and, at 1.7 K, the residual term is dominant. Although having comparable order of magnitude with bulk Nb at zero-field, the residual resistance had a stronger increase with field in the case of the Nb sputtered films (see figure 6), thus resulting in a 'slope' in Q (Q-*slope*). This Q-degradation caused by the

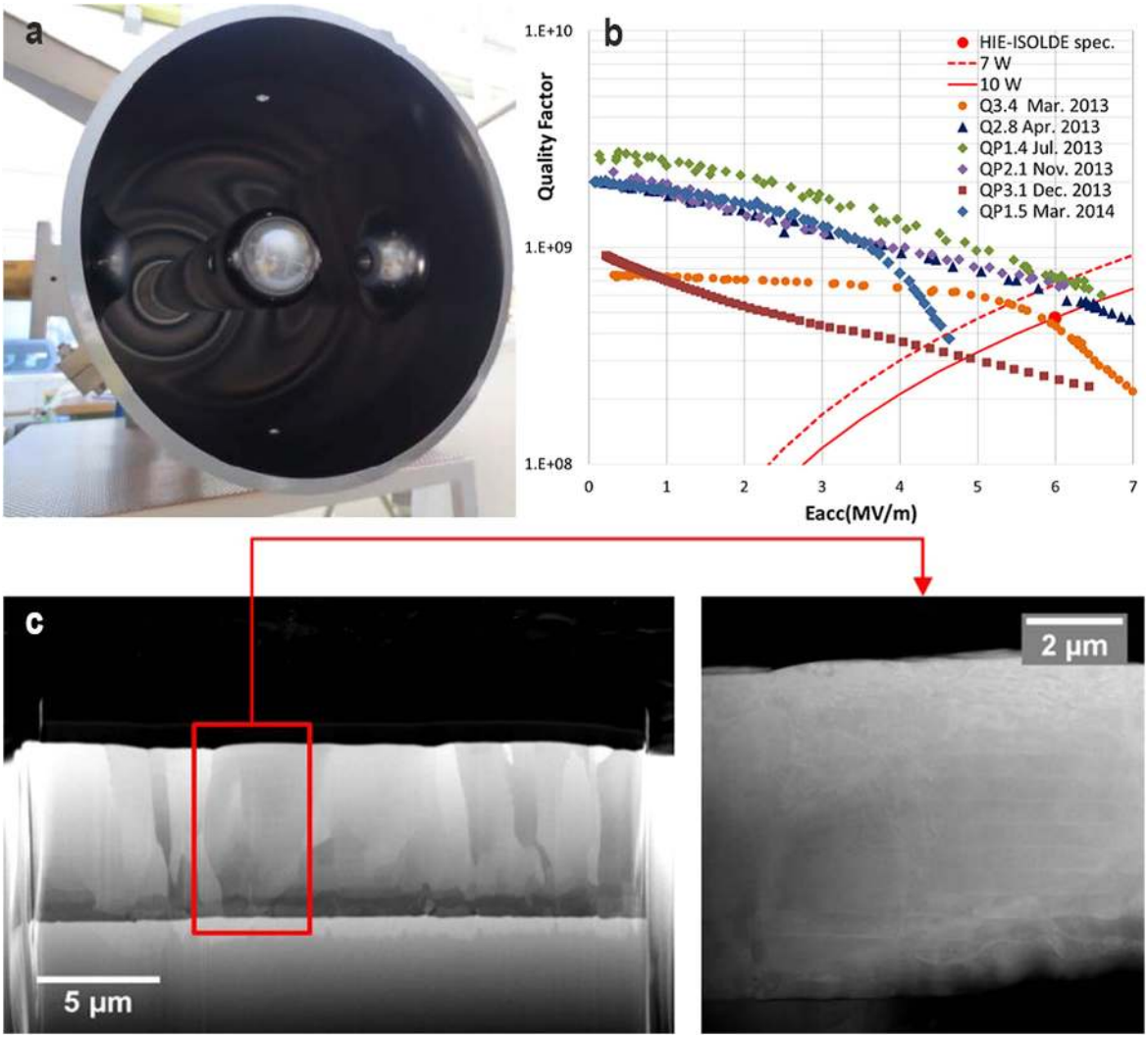

Figure 7. Coated Nb/Cu Hie-Isolde cavity (a); RF performance of HIE-ISOLDE cavities from [27] (b); FIB-SEM cross-section micrograph of an HIE-ISOLDE Nb/Cu film (c) courtesy of Sublet.

increased external RF field actually exists in both bulk Nb and in thin film cavities but for the latter, it limits the cavity operation to relatively low field. This anomalous RF loss is known as the non-quadratic loss (NQL) [28].

Some models predict that such Q-slope is inherent to Nb films due to the limited electron mean free path compared to bulk Nb. This should manifest either in a reduction of H_{c1} and thus nucleation of so-called Abrikosov fluxons [29] at a rather low RF field, effect possibly enhanced by demagnetization due to surface roughness. Other models suggests that the *Q-slope* could manifest itself in a depression of the superconducting gap due to a reduction of the critical superfluid velocity [30, 31], inducing a direct increase of R_{BCS}. Both phenomena are observed in sputtered Nb films. However the relevance of one or the other is *a priori* difficult to estimate. It is then of ultimate importance to study in depth the film material properties and their influence on the films RF performance.

Roughness. Thin films typically replicate the morphology of the substrate they are deposited on. Thus, the roughness of the substrate has a strong influence on the roughness of the film. In magnetron sputtering, shadowing effects during film growth, enhanced by a non-normal angle of incidence [32], can lead to poorly connected Nb film grains. Granularity effects have always been seen as a major source of problems in literature, due to possible losses in weak-links [20] or easier penetration of (Josephson) fluxons [30]. Studies were performed with different substrate roughnesses (hydroformed, spun and electroplated Cu cavities), showing that the smoother substrates led to lower residual losses. Further improvement of the residual losses was achieved by adopting electropolishing which yields a smoother surface finish [22].

Structure. In the framework of the CERN R&D program on Nb/Cu sputtered cavities, films were deposited on a variety of substrates: native Cu oxide, Cu crystalline surface obtained by heat treatment, reverse sputtering (etching) or Cu layer deposition, Nb and oxide free Nb, and various sputtered underlayers (Au, Ti, Sn, Al and Al_2O_3). It was found that all films belonged to one of two families: *standard* films (native Cu oxide, Au, Ti, Sn, Al and Al_2O_3) and *oxide-free* films

Table 2. Film properties for both types of Nb sputtered films (*standard* and *oxide-free*) [34].

	Standard	Oxide-free
RRR	~10	~30
T_c (K)	9.51 ± 0.01	9.36 ± 0.04
Ar cont. (ppm)	435 ± 70	286 ± 43
Texture	(110) Fiber texture	(110), (211), (200) Hetero-epitaxy
Grain size (μm)	0.1–0.2	1–5
λ/λ_{clean}	1.51 ± 0.04	1.04 ± 0.09
H_{c2} (T)	1.15 ± 0.025	0.77 ± 0.01
a_0 (Å)	3.3240(10)	3.3184(6)
Stress (Mpa)	−706 ± 56	−565 ± 78
Strain $\Delta a_\perp/a_\perp$ (%)	0.636 ± 0.096	0.466 ± 0.093

(reverse sputtered Cu, Cu underlayer, heat-treated Cu, oxide-free Nb). The characteristic properties for these two types of films are reported in table 2. The *standard* films exhibited a fine fiber grain structure (figures 8(a) and (c)) with preferential (110) texture. The *oxide-free* films were hetero-epitaxial with equi-axed grains, for which the growth was driven by the underlying Cu structure (figures 8(b) and (d)). In general, the hetero-epitaxial films exhibited material and superconducting properties closer to bulk Nb. However, fluxon-induced and residual RF losses were higher than for the *standard* Nb films [34, 36].

Impurities. A certain number of impurities can be found in Nb sputtered films mainly due to the deposition process and the affinity of Nb for O and H. These impurities can present themselves as scattering centers and thus induce RF losses.

In the magnetron sputtering technique, a sputtering or carrier gas must be used. Thus, atoms of this gas are embedded in the film. CERN conducted detailed investigations [14] of the quantity of gas embedded in Nb/Cu films (for Ar, Kr, Xe, Ne and mixtures) and its effect on their SRF performance as seen in figures 9(a) and (b), for residual and fluxon-induced losses.

The best cavity performances were achieved for films deposited with Kr, combined with substrate electropolishing (see figures 6, 9(a) and (b)). The quantity of residual Kr in these films was about two orders of magnitude lower than for films coated with Ar.

Hydrogen is found to be a primary source of losses in bulk Nb cavities. Similarly, hydrogen trapped in Nb films is a possible cause of Q degradation. The largest sources of hydrogen are the outgassing from the Nb cathode and the Cu substrate during the deposition process and, of course, the residual hydrogen in the vacuum system. The Nb film hydrogen content and its binding state have been measured at CERN for different coating procedures [33, 36]. Despite the efforts to eliminate the hydrogen sources and the use of non-evaporable getters [37], hydrogen reduction was unfortunately not effective.

Though still subject to discussion, oxygen is another suspected source of RF losses [38, 39]. In their analysis of CERN's Nb films data [40] Malev and Weisser proposed that the stimulated desorption mainly contributes to the oxygen and carbon oxide partial pressure to 10^{-7} mbar during the Ar discharge sputtering [41]. However, several analyses show no concentrated oxygen migration to the grain boundary and the interface of the thin film and its substrate [28].

Inter-grain losses. Another potential source of RF losses is inter-grain losses, a basic effect for fine-grained superconductors. Counter evidence for this mechanism comes from the fact that films grown on oxidized Cu have a grain size of 100 nm, but when grown on an oxide-free Cu surface, the grain size is of the order of micrometers. However, larger grain sizes do not seem to have any effect in decreasing the Q-slope. Inter-grain defects can be also generated by impurities (as mentioned above) trapped in the film and surface roughness. Irregularities on the substrate can result in film inhomogeneities. The intrinsic defects are believed to be conducting nanometer size junctions which decrease the critical magnetic field of the superconducting thin film and are similar to the intra-granular weak links in a superconductor [28]. The intrinsic defects can also trap the RF magnetic flux contributing significantly to NQLs.

4.3. Next generation Nb films via energetic condensation

As seen in the previous section, the magnetron sputtering techniques used for SRF Nb/Cu cavities have presented significant limitations which contribute to a poorer RF performance. In recent years, deposition techniques using hyperthermal ions have been developed. These techniques offer increased flexibility and control of the deposition processes, leading to films with improved characteristics.

Control over the deposition process is typically exercised by only three first-order vapor parameters and one first-order substrate parameter. The vapor parameters are the absolute arrival rates of film atoms, the partial pressures of background gases in the chamber, and the energy of the deposition fluxes. The substrate parameter is the substrate temperature. Without energetic atoms, only the substrate temperature influences the processes of physi- and chemisorption, thermal desorption, nucleation, nuclei dissociation, surface diffusion, and formation of specific nucleation sites. Crystalline defects, grains connectivity, and grain size may be improved with a higher substrate temperature, which provides higher surface mobility (the important parameter is the homologous temperature $= T_{substrate}/T_{melting\ of\ film}$). However practical substrates for SRF cavities (Al, Cu) may not allow heating to high enough temperatures. The missing energy may then be supplied by ion bombardment.

Energetic condensation is a deposition process where a significant fraction of the condensing species have hyperthermal and low energies (10 eV and greater). It is characterized by a number of surface and sub-surface processes that are activated or enabled by the energy of the ions arriving at the surface [42–45].

If the incident ions have an energy between the surface displacement and bulk displacement energies, the atom

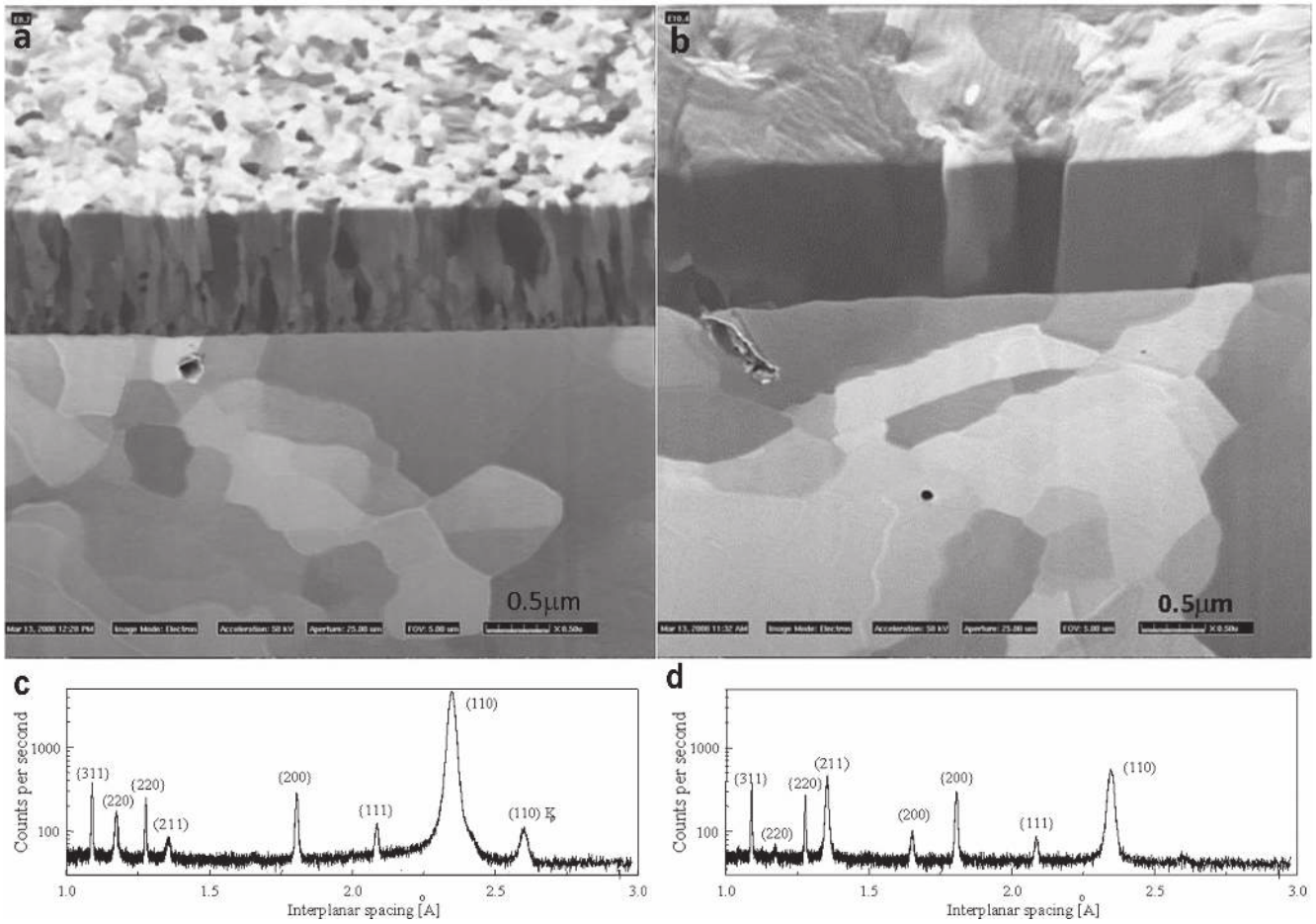

Figure 8. Microstructure for sputtered Nb/Cu films with an oxidized interface (a) and a crystalline Cu interface (b) [36] with the respective Bragg–Brentano spectra (c), (d) from [14], copyright 1999 Elsevier.

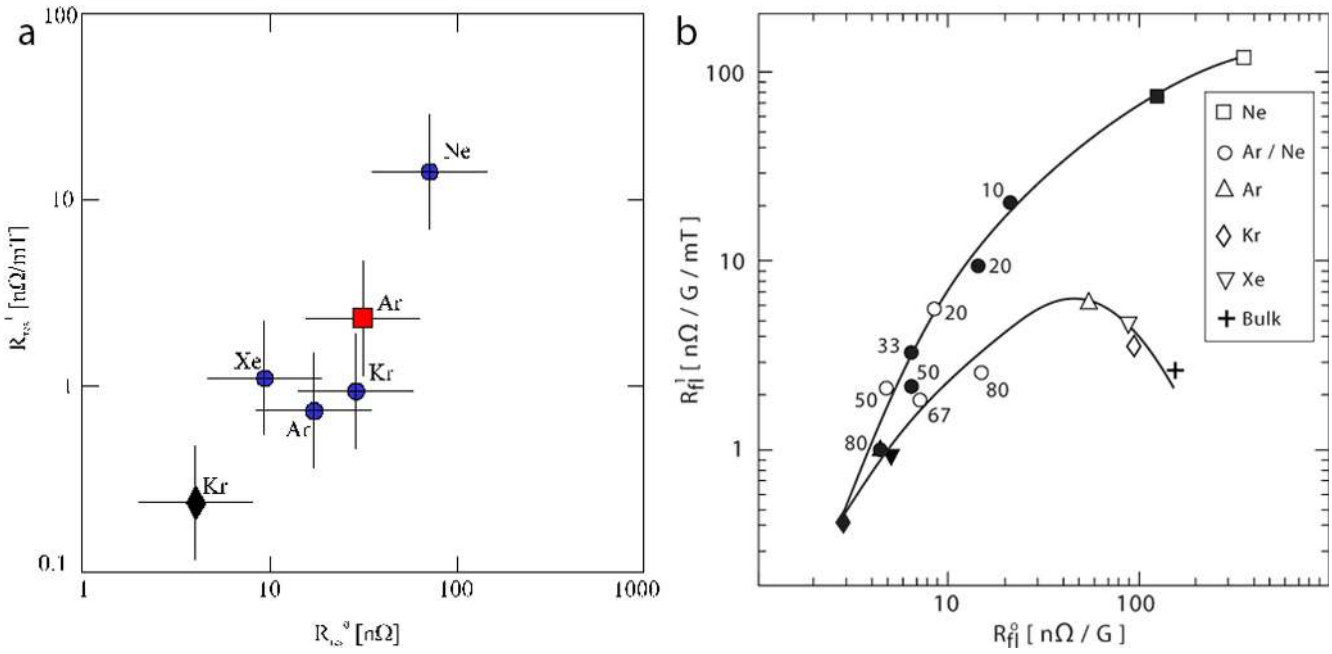

Figure 9. Influence of sputtering gas nature (Xe, Kr, Ar, Ne) on R_{res} for *standard* films coated on chemically etched hydroformed (red, R_a) = 0.8 μm), chemically etched spun (blue, R_a) = 0.2 μm), electropolished spun cavities (black, R_a) = 0.04 μm, absence of etching pits), $R_{res} = R_{res0} + R_{res1}(H_{RF})$ from [22], copyright 2001 Elsevier (a); influence of sputtering gas nature on fluxon-induced losses R_{fl}, $R_{fl}(1.7\ \mathrm{K}) = (R_{fl0} + R_{fl1}H_{RF})H_{ext}$ (b) [34], copyright 2001 Elsevier.

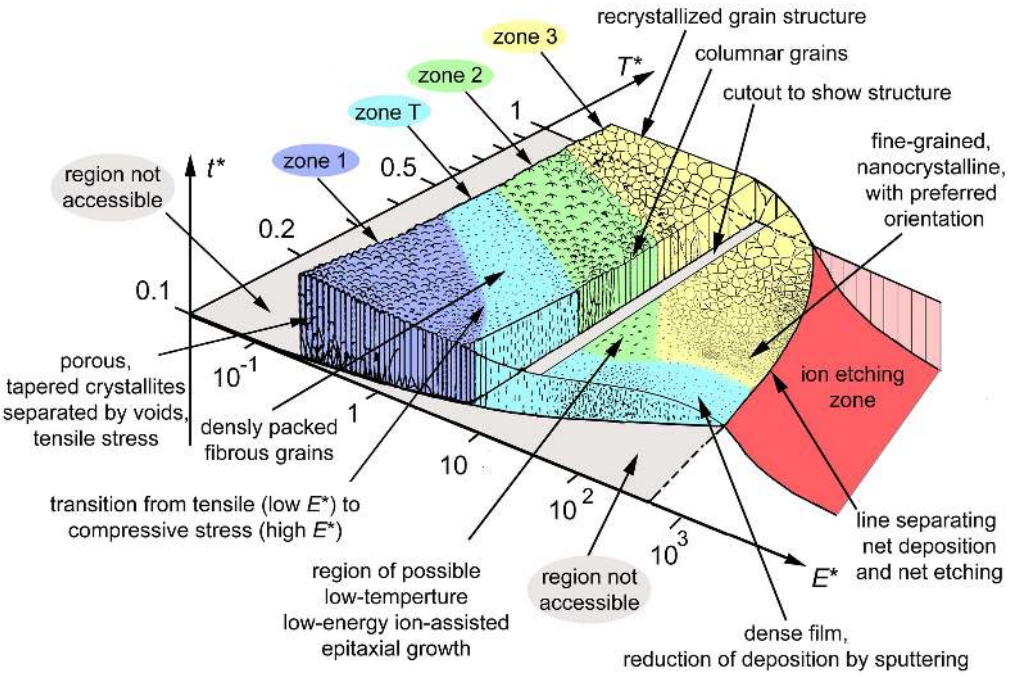

Figure 10. Modified structure zone diagram from [45], copyright 2010 Elsevier.

surface diffusion is promoted without creation of defects in the film bulk, thus promoting epitaxial growth [46].

When the incident ion energy increases beyond the bulk displacement energy (typically 12–40 eV [47]), the ions can be sub-implanted into the surface, generating defects and intrinsic stress followed by re-nucleation [48].

As the energy of these penetrating ions increases, a very short ballistic phase with displacement cascades occurs followed by a thermal spike phase (atomic scale heating). The atoms have a very high mobility in the affected volume, so the thermal spike can be considered as a transient liquid. As soon as atoms have found their place, large amplitude thermal vibrations still facilitate diffusion, especially the migration of dislocations and interstitials and ad-atom mobility on the surface. This favors the annihilation of defects and re-nucleation.

As the kinetic ion energy continues to increase, usually by biasing, the sputtering yield increases, causing a deposition rate reduction (re-sputtering) until the film growth ceases and the surface starts to be etched.

All energy forms brought by the condensing ions to the surface will ultimately contribute to non-local heating of the film, shifting the working point of process conditions to a higher homologous temperature. This can replace conventional heating and produce dense films via enhanced surface mobility at generally low bulk temperature. At higher temperature (higher homologous temperature or temperature increase due to the process itself), the grains are enlarged because the ad-atom mobility increase dominates over the ion-bombardment-induced defect increase and re-nucleation rates [49]. The relationship between the coating morphology, the substrate temperature, kinetic energy of the ions, and the deposition rate is summarized in the revised structure zone diagram proposed by Anders (figure 10) [45].

In summary, these competing processes due to the additional energy provided in energetic condensation techniques can induce the following changes to the film growth process:

- Residual gases are desorbed from the substrate surface.
- Chemical bonds may be broken and defects created thus affecting nucleation processes and film adhesion.
- Film morphology changes.
- Microstructure is altered.
- Stress in the film alters.

As a result of these fundamental changes, energetic condensation allows the possibility of controlling some of the film properties. The density of the film may be modified and the crystal orientation may be controlled to give the possibility of low-temperature epitaxy.

Energetic condensation is implemented in three main groups of techniques developed for *next generation* SRF Nb films: vacuum arc deposition [50, 51], energetic condensation via electron cyclotron resonance (ECR) plasma [52] and high power impulse magnetron sputtering (HIPIMS or also HPPMS) [53].

4.3.1. Vacuum arc deposition. Vacuum arc deposition has been developed extensively and is described in details in [54, 55]. In this coating technique, an electric arc is established over the cathode's surface by a suitable trigger (high voltage or laser pulse). The arc is sustained by an adequate power supply, with the plasma plume containing Nb atoms at such a high density that they are fully ionized. The technique provides a high coating rate, and of course the

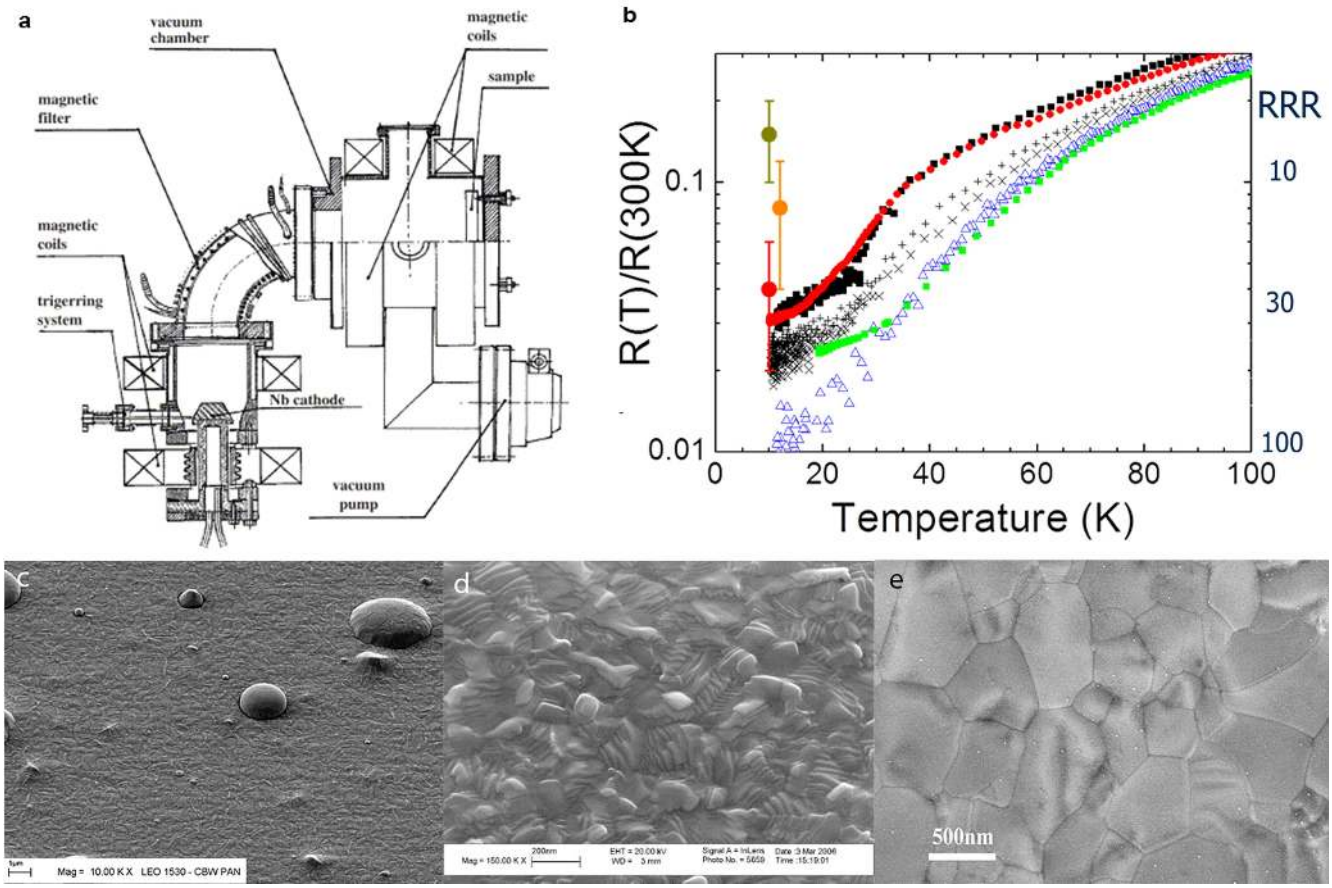

Figure 11. Schematic for the vacuum arc deposition system for the ARCO project [59], copyright 2006 Elsevier (a); resistivity curves and associated RRR values (circles) for different UHVCA Nb films on Al_2O_3 and Cu (b); SEM micrographs of unfiltered (c), filtered (d) and filtered pulse-biased (d) UHVCA Nb/Al_2O_3 films [57], copyright 2005 IOP Publishing Inc.

coating flux can be attracted at the desired energy towards the substrate. The typical Nb ions kinetic energy can be higher than 100 eV and are multiply charged (the mean ionization for Nb is +3) so the average kinetic energy of the Nb atoms reaching the substrate can reach up to 350 eV for a −80 V bias voltage. The ionization state +3 also provides an additional potential energy of about 46 eV [56] which is released in the growing film and the substrate as ions are neutralized.

INFN 'Roma II' and the Soltan Institute for Nuclear Studies (Poland) formed, a few years ago, a collaboration to investigate the feasibility of a vacuum arc deposition (UHVCA) technique for Nb/Cu cavities [57, 58]. A schematic of the filtered UHVCA deposition system is given in figure 11(a).

Nb coatings have been performed on Al_2O_3 and Cu samples and have been fully characterized. The Nb/Cu samples have shown good quality Nb with RRR values ranging from 20 to 60 (figure 11(b)) and very good substrate adhesion. The transition temperature ranged randomly from 8.7 to 9.26 K [59]. The depositing energy varies from 10 to 100 eV yielding a crystallite size range up to several microns (figures 11(c)–(e)), to be compared to a few hundred nm in the case of sputtering. The films are typically free from intra-grain defects and strain, major sources of electron scattering in sputtered films.

A strong disadvantage of this technique is however the formation of macro-particles (figure 11(c)) because of the explosive nature of the process. Magnetic filtering and steering of the ion flux is then needed, in order to remove macro-particles from the flux and to obtain a defect-free coating (figures 11(d)–(e)), adding complexity to the coating system [60]. A filtered UHV arc coating system for RF cavities, using two symmetrical cylindrical arc sources was built and a couple cavities were coated [61]. However, the best result on small samples was not reproduced on larger surfaces.

A similar technique, named coaxial energetic deposition (CED^{TM}), has also been implemented at Alameda Applied Sciences, Inc. (AASC, CA, USA) (figure 12(a)). In this case also, high quality Nb films on small samples (figure 12(b)), mainly MgO, have been produced [62] with values up to 500 (figure 12(c)). First trials on cavities [63, 64] have been performed with Q values below 10^9. These coated cavities often suffered from significant delamination of the film from the substrate. However, these first results are not necessarily due to a limitation of the technique but most likely due to the current limitations of the experimental setups. Steps are being implemented to improve the experimental conditions.

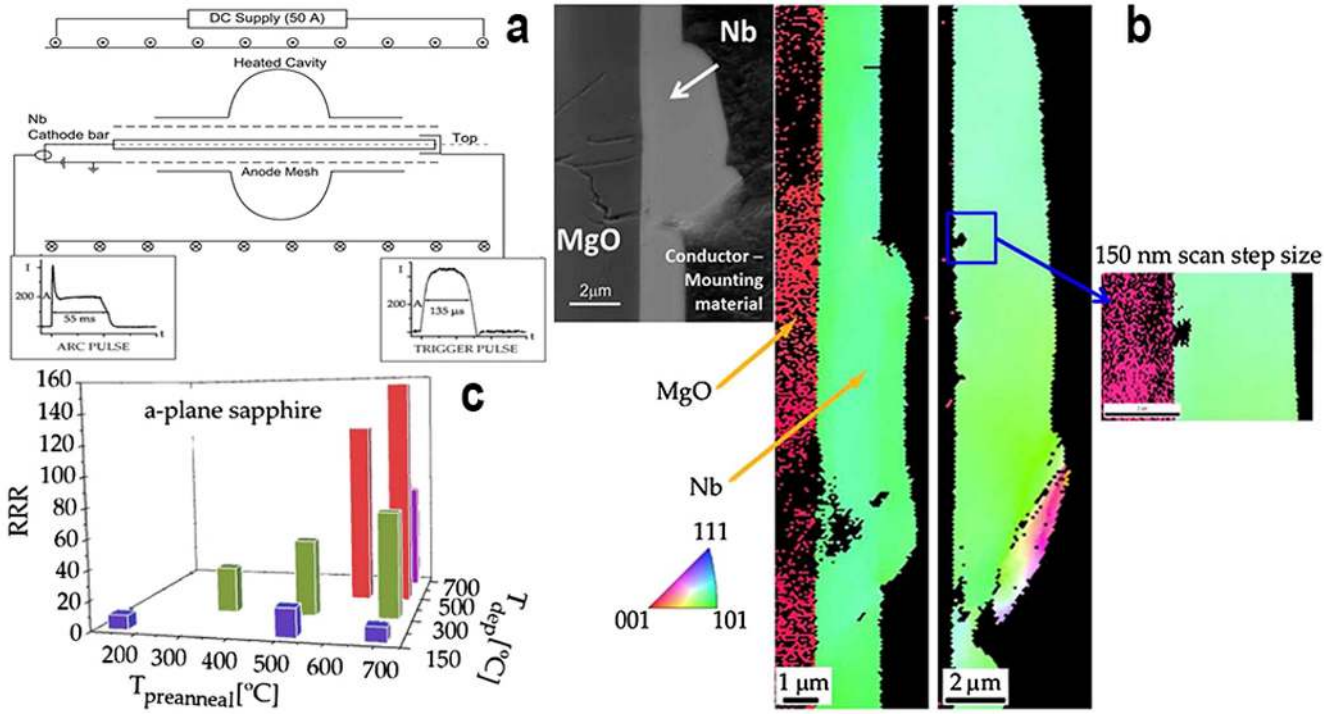

Figure 12. Principle of the CED^{TM}deposition (courtesy Krishnan) (a); SEM cross section and TKD (transmission kikuchi diffraction) for a Nb/MgO film (b); RRR evolution for Nb/Al_2O_3 as a function of bake and coating temperatures (c) from [63], copyright 2012 The American Physical Society.

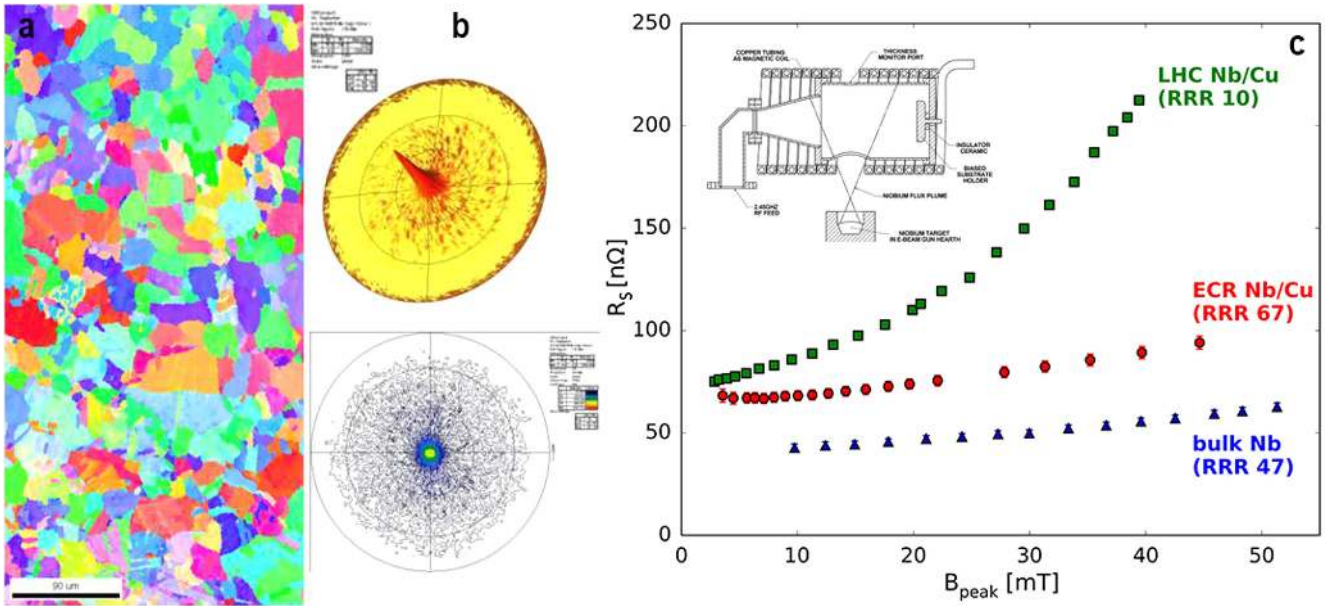

Figure 13. EBSD map (a) and XRD pole figures (b) for an ECR Nb/Cu film; surface resistance of an equivalent ECR Nb film at 400 MHz and 4 K, compared to sputtered Nb/cu and bulk Nb [66], courtesy of Aull.

4.3.2. ECR plasma. Another technique of energetic condensation is based on creating, under UHV conditions, an ion plasma via ECR [52]. The principle is to first produce with an electron beam gun a neutral vapor of Nb that is introduced in the ECR chamber. When perpendicular magnetic (874 G) and RF electrical (2.45 GHz) fields are applied to the chamber, the residual electrons are accelerated to their cyclotron resonance and ionize the neutral Nb vapor. The ions generated are almost only singly charged and have an inherent energy of 64 eV. These ions can be further accelerated towards the substrate by applying a bias voltage, allowing control over the incident ion energy. The distinct advantages of this technique are the production of a high flux of singly charged ions with controllable kinetic energy in an

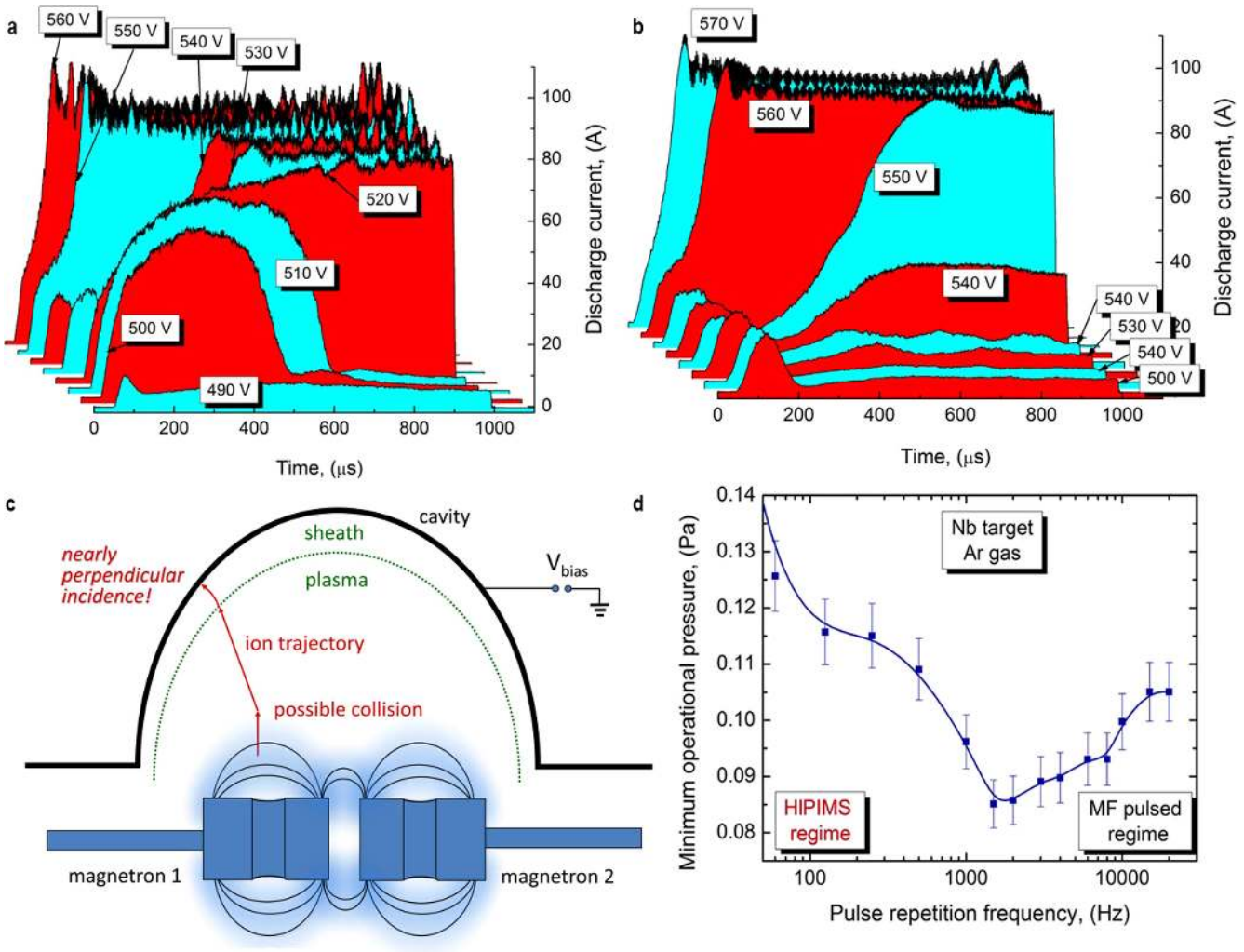

Figure 14. Characteristic HIPIMS current pulses for a 50 mm Nb target operating in 0.5 Pa of Ar (a) and Kr (b); minimum operational pressure of a Nb HIPIMS discharge in Ar with 5 cm magnetron (applied voltage 1000 V, pulse length 30 μs, maximum average power 1 kW) (c); schematic of the LBNL dual magnetron HIPIMS deposition system for 1.3 GHz cavities coating (d); from [71].

ultra-high vacuum environment and the freedom from macro-particles. ECR Nb deposition has been studied on a variety of substrates, from highly crystalline to very rough polycrystalline and amorphous surfaces, from Cu to insulators, at various temperatures and bias voltages [65]. It has been demonstrated that the Nb film quality can be tuned by varying substrate temperature and bias voltage, achieving RRR values similar to bulk Nb values (up to 700). The Nb films typically exhibit excellent material properties (figures 13(a) and (b)) and enhanced adhesion to the substrate. The content of impurities such as H is several order of magnitudes lower than for bulk Nb [65].

The 4 K and 400 MHz performance of an ECR Nb/Cu film is shown in figure 13(c) along with a reactor grade bulk Nb QPR sample (RRR 47), and a typical LHC magnetron sputtered cavity (RRR $\sim$ 10) [66]. As can be observed, R_{res} at low field for the ECR film is comparable to the LHC sputtered cavity, but the slope of R_S with field is comparable to the bulk Nb of similar RRR. In this case, the relatively high R_{res} may be due to contamination from e-beam welding of the sample to the support structure, performed post-deposition.

4.3.3. High power impulse magnetron sputtering (HIPIMS) development for Nb/Cu cavities. HIPIMS is actually an array of deposition techniques which is seeing extensive development in the industry. The characteristics of the films produced can be of great benefit in the development of Nb film coatings for SRF application. Several institutions (Jefferson Lab, Lawrence Berkley National Laboratory (LBNL) and CERN) are applying this technique to SRF cavities.

The HIPIMS process has been the object of extensive plasma studies applied to a variety of materials at LBNL in the group of Andre Anders [67, 68]. Various experiments are carried out in a general-use chamber to explore the plasma physics and characteristics of the HIPIMS process, especially applied to Nb (the characteristic HIPIMS current pulses for Nb with Ar and Kr as carrier gas are shown in figures 14(a)

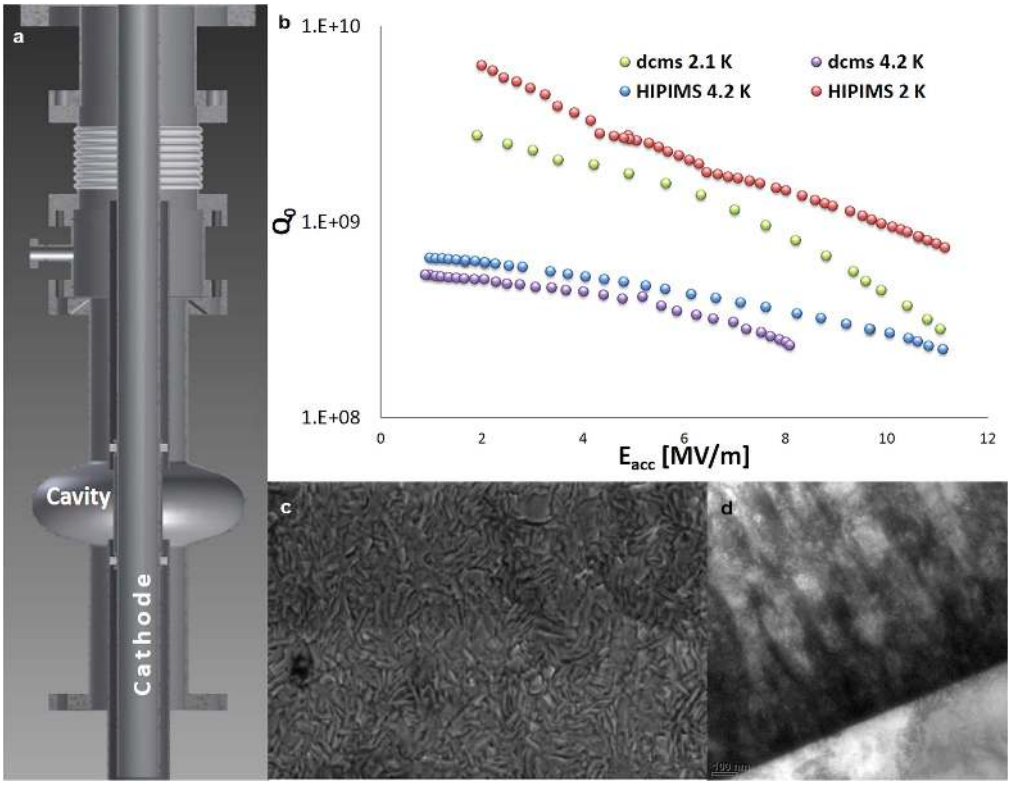

Figure 15. HIPIMS cavity deposition system used at CERN (a); quality factor at 4.2 and 2.1 K of two elliptical single cell cavities, produced by dc-MS and HIPIMS sputtering (b); SEM (c) and TEM cross-section (d) for a HIPIMS Nb film [74, 75]; courtesy of Terenziani and Calatroni.

and (b)) and other SRF materials. The possibility of 'gasless' self-sputtering [69] of Nb, e.g. a HIPIMS mode in which the sputtered atoms fill in the role of a process gas, was explored. Thus no argon (Ar), krypton (Kr) or any other gas is needed, eliminating the issues related to noble gas inclusion, which would be a big progress compare to dc magnetron sputtering (dc-MS). Such 'gasless' self-sputtering has been demonstrated for HIPIMS using high sputter yield materials such as copper [70]. In the case of Nb [71], the sputter yield is not sufficient to produce enough 'Nb gas'. Rather, noble process gas is always needed to obtain HIPIMS pulses. This led into the exploration of the minimum pressure needed to obtain a HIPIMS Nb discharge [72]. It was found that, due to some 'residual plasma' of the previous pulse, the pulse repetition rate is an important parameter that allows pressure reduction while still maintaining a stable and reproducible operation.

Another recent development of the HIPIMS process consists in superimposing a mid frequency (MF) discharge in between the HIPIMS pulses to lower the frequency pulses of the HIPIMS pulses. Though they do not depend on MF pulse pattern, the HIPIMS pulses can be spaced as far (or close) in time as desired as long as the MF discharge is present. Conditions are found where the species in the plasma are largely dominated by Nb^+ [73].

In parallel to the exploration of HIPIMS process for the development of SRF materials, a cavity deposition concept was implemented (see schematic in figure 14(d)) with a set of two, movable cylindrical magnetrons. The two magnetrons are mounted on movable arms, as shown in figure 14(c), to uniformly coat the inside of the cavity while slowly traveling through it. Their travel is synchronized by computer-controlled stepper motors. The use of two magnetrons allows the option of biasing the cavity for film optimization. The concept is to use one target as the cathode, and the other as the anode. The polarity of the targets is alternated at a frequency typical for HIPIMS, so the cavity does not participate in the discharge process and can be biased using another, independent power supply. The deposition rate can be also doubled by using each of the magnetrons at its maximum power rating. This leads to a shorter process time and a reduced incorporation of residual gas contaminants. No coated cavities have been produced yet.

HIPIMS plasma with Nb studies and development of the technique for the coating of 1.5 GHz Nb/Cu cavities are also on going at CERN in collaboration with Sheffield Hallam University [74] and at Jefferson Lab. The CERN HIPIMS coating system described in details in [75] has a vertical cylindrical magnetron configuration (figure 15(a)). It is built on the basis of the dc cylindrical magnetron coating system for 1.5 GHz Nb/Cu cavities used in previous studies [14]. It is an all-metal UHV system with the cavity being part of the vacuum system. The base pressure of the system is in the 10^{-10}–10^{-11} mbar range. The cavity beam pipes are coated in sequential steps by dc-MS, while the cell is coated either by HIPIMS or by dc-MS. The coatings are performed in a 10^{-3} mbar range Kr atmosphere. The produced films are fine grained but dense (figures 15(b)–(d)).

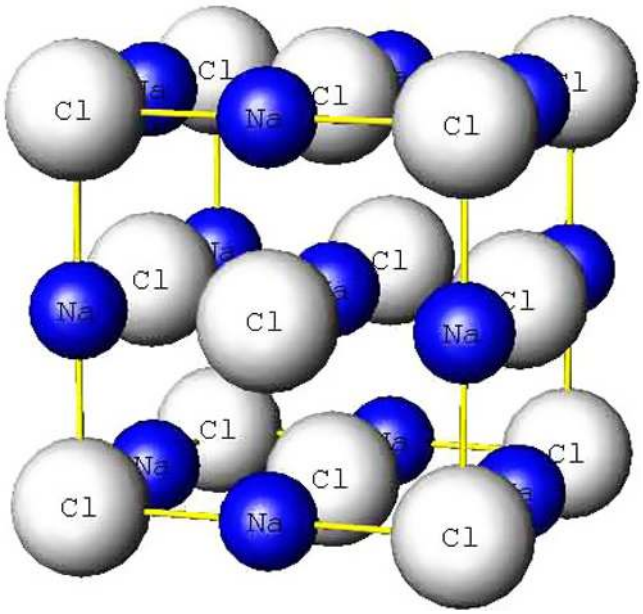

Figure 16. NaCl structure from [77]. In B1 compounds, the metallic atoms form an fcc lattice (Cl) and the non-metallic atoms occupy the octahedral interstices (Na).

Some 1.5 GHz Cu cavities have been coated with both HIPIMS and dc-MS. Figure 15(b) shows the quality factor curves at 4.2 and 2.1 K for a dc-MS cavity and HIPIMS cavity, both coated with Kr. These very preliminary results show an improvement in the performance of Nb films coated by HIPIMS compared to dc-MS. The ongoing studies should yield more RF results in the near future.

5. Nb B1-compounds

B1 compounds have a NaCl structure where metallic atoms A (Cl) form a face centered cubic (fcc) lattice and non-metallic atoms B (Na) occupy all the octahedral interstices (figure 16). These compounds are characterized by the fact that they have a certain amount of vacancies, usually randomly distributed throughout the lattice [76]. The superconducting properties of B1 compounds are very sensitive to deviation from the stoichiometric composition.

Among all the superconducting B1 compounds, only a few nitrides and carbides of the IV, V, VI group transition metals have a T_c higher than Nb, as reported in [76], namely NbC (12 K), TaC (10.35 K), WC (10.0 K), ZrN (10.7 K), NbN (17.3 K) and MoC (14.3 K).

5.1. NbN

NbN is one of the B1 binary compounds with the highest critical temperature. For this reason, it has been occasionally tested for SRF cavity applications. The phase diagram of the binary system Nb-N up to $N/Nb = 1$ includes many different phases [78, 79], characterized by different T_c [80]. The B1-NbN superconducting phase of interest is the cubic δ-phase for which $T_c = 17.3$ K and the lattice parameter is 4.388 Å. This phase is only thermodynamically metastable at room temperature and T_c is very sensitive to nitrogen stoichiometry.

Various attempts have been made to produce NbN cavities by thermal diffusion [81–83] or reactive magnetron sputtering. For NbN made by thermal diffusion of N into Nb at 1400 °C followed by rapid quench cooling, surface resistances of 1.3×10^{-6} Ω and 1.3×10^{-10} Ω were calculated from TE_{011} measurements at 7.9 GHz and respectively at 4.2 K and 1.8 K [84]. NbN was produced by reactive magnetron sputtering [85], even when deposited at relatively low temperature (600 °C), with good superconducting properties ($T_c = 17$ K, figure 17(a)), a low secondary emission coefficient and very stable surface properties. However, the resistivity of NbN in the normal state was found to be anomalously high (see figure 17(b)) and the RRR is very low (~1). In sputtered films, the δ-phase is often found to be mixed with other phases. The films are columnar, with weakly bounded grains separated by strong boundaries consisting of voids, normal conducting areas of Nb, and Nb-dissolved gas composite phases. Even with no grain boundaries and only the δ-phase present, the resistivity is still high due to the presence of both metallic and gaseous vacancies randomly distributed in both sublattices, in amount of 1.3%. The equiatomic composition is not $Nb_{1.0}N_{1.0}$ but $Nb_{0.987}N_{0.987}$.

5.2. NbTiN

The ternary nitride NbTiN presents all the advantages of NbN but shows more metallic electrical conduction properties with higher titanium (Ti) percentage. Ti is a good nitrogen getter, so the higher is the Ti composition, the lower is the number of vacancies. In contrast with NbN, the B1-TiN phase is stable at room temperature ($T_c = 5$ K and $a = 4.24$ Å). The two nitride phases are completely miscible [86] resulting in a superconducting ternary NbTiN cubic phase which remains thermodynamically stable at room temperature. T_c is slightly higher (17.8 K) but, as with NbN, N stoichiometry is critical to obtaining the right superconducting phase. The commonly used techniques to produce NbTiN are reactive diffusion of NbTi sheets by high temperature heating in nitrogen atmosphere [84, 86] and reactive sputtering [87, 88].

Figures 18(a) and (b) show the T_c and the low-temperature normal resistivity as a function of Ti composition for NbTiN samples produced by reactive sputtering in Ar/N_2 mixture in a dc Triode Magnetron Sputtering system at 600 °C and 200 °C [88]. The resistivity is found to be lowered with increasing Ti content.

NbTiN films were also deposited on Cu disks by reactive magnetron sputtering and tested at 4 GHz in a cylindrical TE_{011} cavity at CEA Saclay [89, 90]. The best results show RF field levels of 35 mT, a low R_s (<50 nΩ at 1.6 K) with a small R_{BCS} (figure 19). Additionally, it was observed that R_s decreases when the coating is performed with a bias voltage from −50 to −100 V. Some attempts were made to deposit 1.5 GHz Cu cavities but no RF measurements were performed due to film blistering on a large area of the cavities.

NbTiN was also investigated at CERN [91, 92] on samples and 1.5 GHz Cu cavities coated by reactive

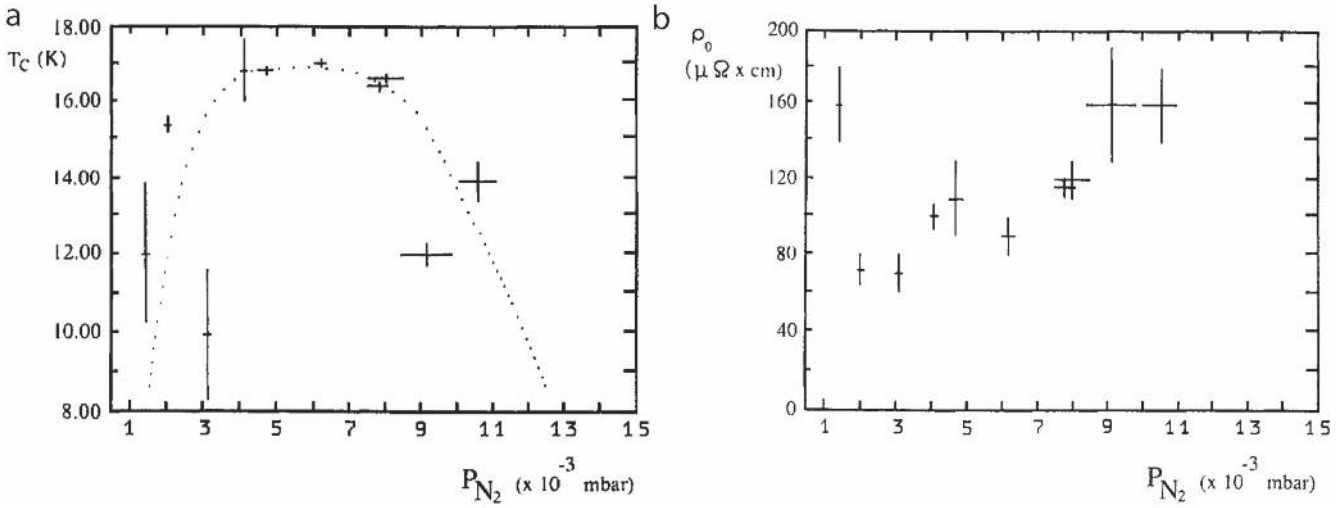

Figure 17. T_c (a) and residual resistivity ρ_0 (b) as a function of N_2 partial pressure P_{N_2} for NbN films produced by reactive magnetron sputtering, from [85], copyright 1988 IOP Publishing Inc.

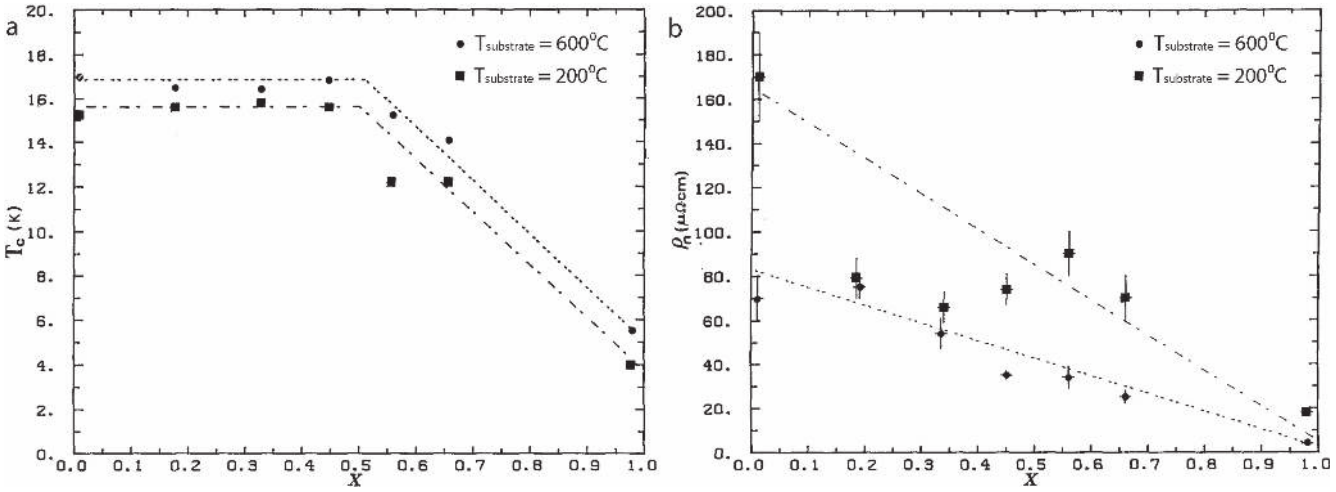

Figure 18. T_c (a) and low-temperature normal state resistivity ρ_0 (b) as a function of the Ti composition X for $(Nb_{1-x}Ti_x)N$ films deposited at $T_{substrate}$ = 600 °C (circles) and $T_{substrate}$ = 200 °C (squares) by reactive sputtering, from [88], copyright 1990 Springer US.

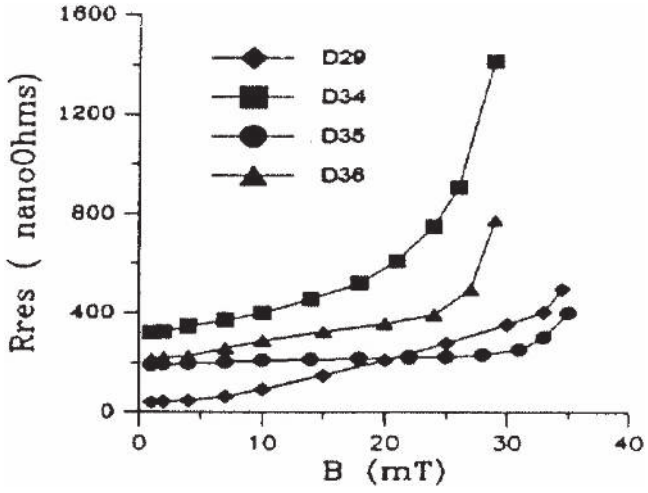

Figure 19. Surface resistance measured at 4 GHz and 1.6 K for NbTiN/Cu films deposited by reactive magnetron sputtering [90].

cylindrical magnetron sputtering. The best cavity results were obtained for a thicker film (4.3 μm) and a lower deposition temperature (265 °C). The measured surface resistance was 330 nΩ at 4.2 K, with a Q-value at zero field higher than for bulk Nb cavities. However, for the few NbTiN/Cu cavities ever coated, the maximum accelerating field was limited under 10 MV m^{-1}.

6. A15 compounds

A detailed review of A15 compounds for RF applications has been given by Sarma in [93], and Stewart [94]. Among the fifty A15 compounds found, the highest T_c (15–20 K) are found among Nb and V based compounds, like Nb_3Sn, Nb_3Al, Nb_3Ge, Nb_3Ga, V_3Si. Although they have the highest transition temperatures, Nb_3Ge and Nb_3Ga do not exist as stable bulk materials for the 3:1 stoichiometry. Bulk Nb_3Al is

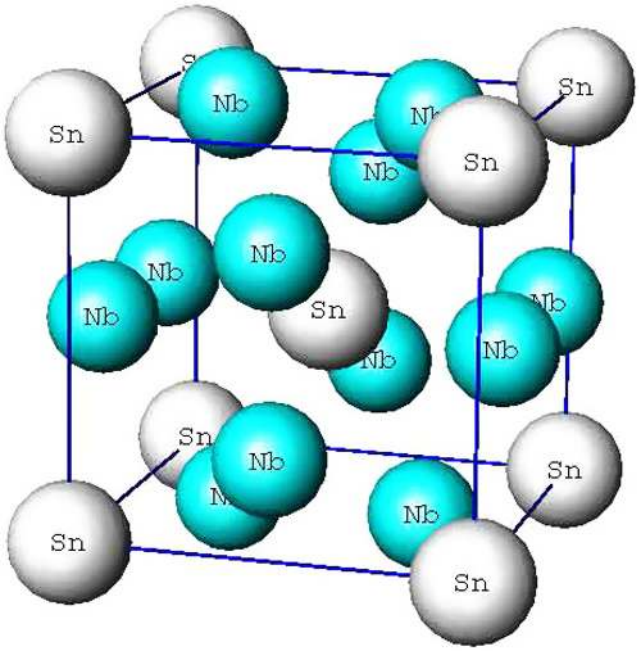

Figure 20. A15 Structure with A_3B composition [77], pictured here for Nb_3Sn.

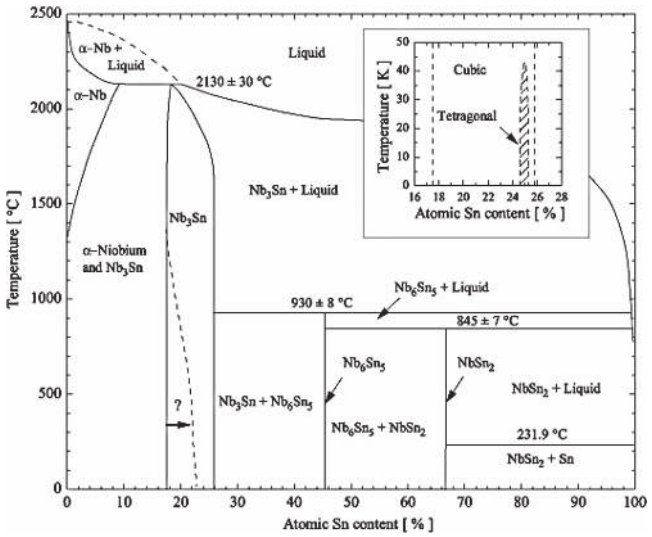

Figure 21. Nb–Sn system phase diagram from [96], copyright 2006 IOP Publishing Inc.

stable only at high temperature (1940 °C), causing excessive atomic disorder. However, thin Nb_3Al films have been successfully produced by various deposition methods. The production of these materials typically requires non-equilibrium processes. On the other hand, Nb_3Sn, V_3Ga, V_3Si are stable bulk materials and have a high T_c. Another A-15 compound of interest is Mo_3Re.

6.1. A15 structure

The study of A15 compounds began intensively in 1953 with Hardy and Helm's discovery of superconductivity in V_3Si with $T_c = 17$ K [95]. The cubic A15 structure, pictured in figure 20 for Nb_3Sn, is also called β-W and the prototypical A15 compound is the non-superconducting Cr_3Si. Although there are often variations of stoichiometry, the ideal formula unit is A_3B where A atoms are transition elements of groups IV, V or VI. B atoms can be non transition or transition elements (mainly from group VIII) [76] and form a bcc (body centered cubic) lattice. As shown in figure 20, a typical feature of the A15 structure is that A atoms form orthogonal chains bisecting the faces of the bcc unit cell, with twice the periodicity of the cubic unit cell. The distance between A atoms within a chain is the shortest distance between atoms in the A-15 structure and is shorter than that between A atoms belonging to different chains. The transition temperature of most A15 compounds is strongly influenced by the linear chain integrity or the degree of long range crystallographic order. T_c is usually maximized for compounds in which the B atom is not a transition metal.

6.2. A15 material preparation

A15 compounds are intermetallic compounds and are extremely brittle in the bulk form, so SRF structures based on bulk A15 compounds cannot be formed. The A15 compound should be produced as a thin layer on the inner surface of the already formed structure. Over the years, various techniques have been extensively developed for HTS wire applications. Although the material characteristics needed for SRF applications are very different from HTS wire applications, some of these techniques can be considered. A versatile technique is sputtering using a target with the correct stoichiometry, usually prepared by powder sintering. The stoichiometry, substrate temperature, deposition rate, and film thickness can be varied independently. Difficult materials such as Nb_3Ge or V_3Si have also been successfully synthesized by co-sputtering, i.e. by sputtering simultaneously two constituents on a temperature controlled substrate. The achieved composition is dependent on the relative positions of the target and the substrate. The perfect stoichiometry can then be obtained by manipulating these positions. However, the control of the stoichiometry may be difficult over large areas like for accelerating cavities, especially if the stoichiometry range for the A15 phase is narrow. metal organic chemical vapor deposition (CVD) is a particular case of CVD in which the precursor is a metallorganic compound. In this process, one or more precursors, present in vapor phase, chemically react and form a solid film on a substrate at the appropriate temperature. The deposition rate and the structure of the film depend on the temperature and the reagent concentration. The control of the temperature and gas flow uniformity over the entire cavity surface may be difficult with complex geometries. Thermal diffusion is a technique that has been proven successful for magnet conductor applications. It can be easily implemented with equipment much simpler than that required for sputtering and CVD techniques.

6.3. Nb_3Sn

The A15 phase for the Nb–Sn intermetallics system is in the composition range of 18–25 at% Sn (figure 21). The superconducting parameters, T_c, Δ, H_{c2}, depend strongly on the Sn

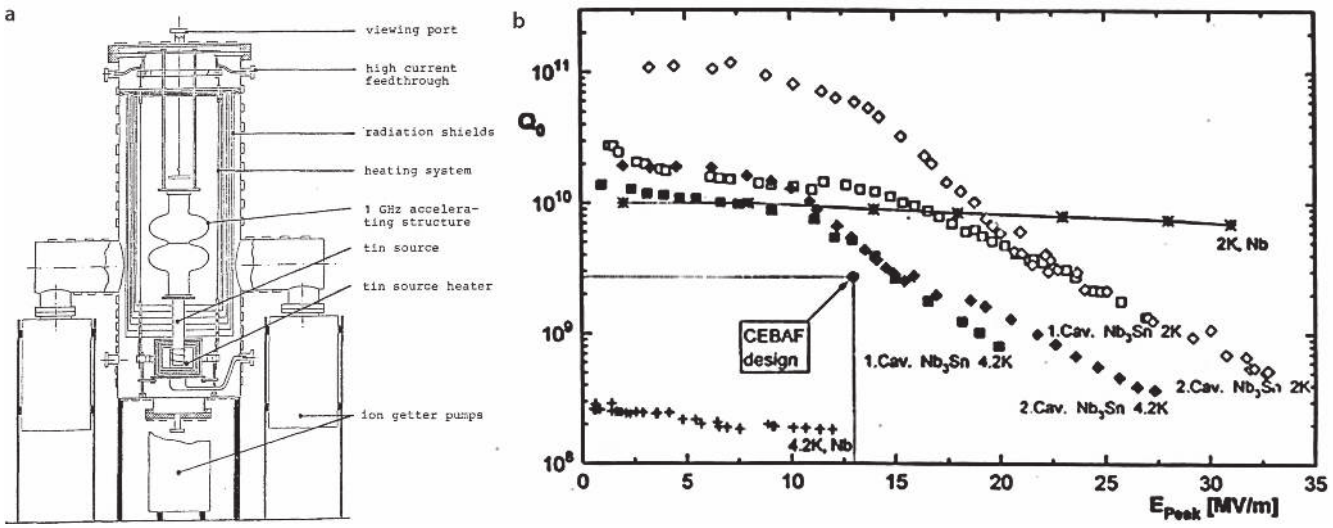

Figure 22. Vapor diffusion setup for Nb_3Sn formation at Wuppertal University (a). Q versus E_{peak} curves at 4.2 and 2 K of the first Nb_3Sn coated 1.5 GHz single cell cavities in comparison to CEBAF bulk Nb cavities [7, 100] (b).

content [96]. Close to stoichiometry (24.5 at% Sn) and as a result of perfect ordering in the stoichiometric phase, ρ_n drops below 20 $\mu\Omega$ cm. R_{BCS} for Nb_3 Sn has then the potential to be much lower and Q much higher than for Nb.

A systematic study on Nb_3Sn was carried out at Wuppertal University in the late 80s [97–100]. In this framework, 1.5 GHz Nb_3Sn cavities were obtained through Sn vapor phase diffusion at high temperature (>1200 °C). A few microns thick Nb_3Sn films were deposited on the inner surface of Nb cavities exposed to Sn vapor (10^{-3} mbar) in an UHV furnace at temperatures between 1050 °C and 1250 °C (figure 22(a)).

The RF performance of these cavities was measured and compared to bulk Nb cavity performance at 4.2 and 2 K (figure 22(b)). High Q-values were retained up to a peak field E_{peak} of 15 MV m^{-1} before Q-drop occurred. The highest E_{peak} achieved was around 30 MV m^{-1}. An attempt was also done with a 5-cell 1.5 GHz cavity which achieved $Q_0 \sim 10^9$ and $E_{acc} = 7$ MV m^{-1} ($E_{peak} = 16$ MV m^{-1}) with $Q = 8 \times 10^8$. Despite these encouraging results, this R&D program stopped in the mid-90s as research efforts shifted to the then newly discovered high-T_c cuprates.

In the recent years, interest has re-emerged in different institutions around the world. Nb_3Sn programs are now on going at Cornell [101], and Jefferson Lab [102] using some variations of the Sn vapor diffusion technique. These programs aim at building on the Wuppertal results while understanding the seeding and growth of Nb_3Sn on bulk Nb surfaces with material and superconducting properties investigations [103].

In general, the Nb_3Sn films produced exhibit good material quality with Sn content of about 25%, T_c from 16 to 18 K, Δ from 2.7 to 3.2 meV (figures 23(a)–(c)) [103]. A certain number of cavities have been produced [102, 104]. Coating results are typically reproducible for the same cavity Nb substrate, but they can vary significantly between different cavities. A few cavities have (see figure 23(d)) shown very good RF performance at 4.2 K with a moderate Q-slope. However, the RF performance can often be limited by a strong Q-slope, very much like the Wuppertal results, and early quenches. These issues, which are yet to be understood, could be due, for example, to the presence of Sn-depleted regions in or close to the RF-probed depth.

A few years ago, the liquid surface diffusion process commercially used for producing Nb_3Sn tapes [95] was modified to produce Nb_3Sn films for SRF applications at INFN-LNL, Italy in the group of Palmieri (figure 24(a)). The so-called '*hybrid liquid diffusion*' process [106] produced Nb_3Sn films with good superconducting properties and $T_c = 17.3$ K with $\Delta T_c = 0.16$ K (figure 24(b)). The process consists first of dipping the substrate in a liquid Sn bath at a temperature higher than 930 °C (to ensure a pure Nb_3Sn phase). The sample is then removed from the bath and annealed in Sn vapor at the same temperature to diffuse the outer layer of Sn in the bulk. Finally, the sample is annealed in an Sn free environment to increase the grain size and favor perfect ordering. No evidence of the presence of Sn-rich phase or residual Sn on the sample surface was found.

Another approach investigated in the same group was through multilayer coating [106] where alternate layers of Nb and Sn are sputtered and subjected to reactive diffusion at 975 °C. A sharp transition around 17 K has been obtained with this method.

Both techniques were applied to coat 6 GHz cavities. However, the results were non-conclusive [106].

Other techniques for synthetizing Nb_3Sn are currently emerging. In one case, Nb_3Sn is electro-deposited from an ionic liquid composed of $SnCl_2$, $NbCl_5$ and BMIC (1-butyl-3-methylimidazolium chloride) at low temperatures (100 °C–130 °C) [107]. This method aims at forming directly Nb_3Sn coatings in molecular form on any conductive substrate without the need of a high temperature post-annealing. In the other case, Nb_3Sn compound is formed on the bulk Nb substrate by the electrodeposition and thermal annealing of a Sn

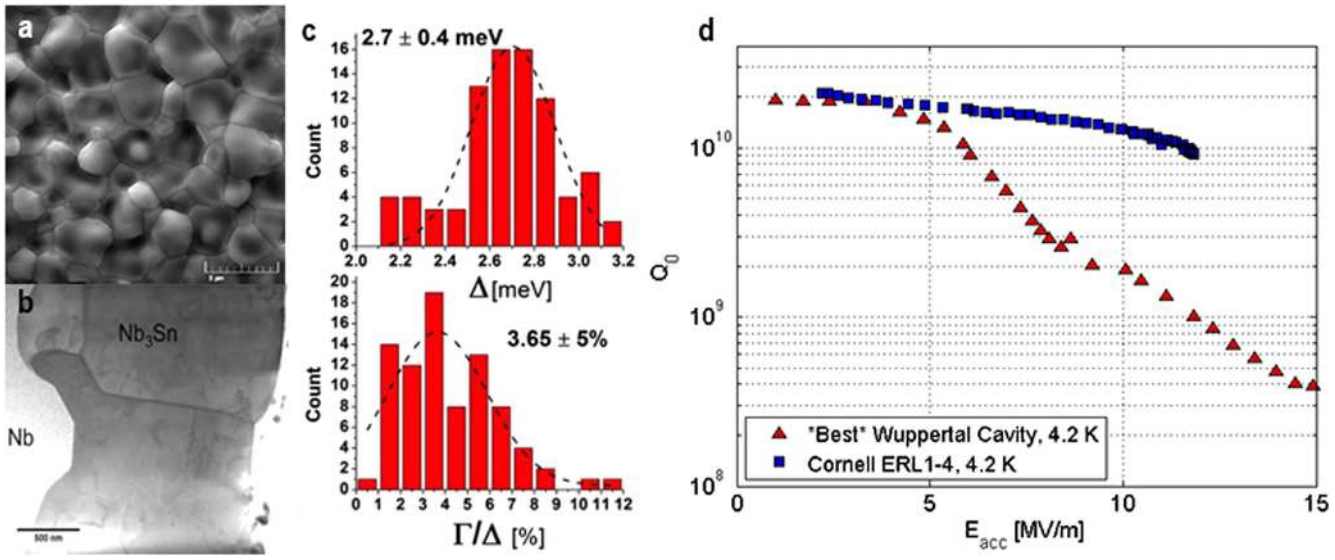

Figure 23. SEM (a), TEM cross section (b) and gap measurement by point contact tunneling (PCT) (c) for a typical Nb_3Sn film, from [103], copyright 2015 AIP Publishing LLC; Cornell Nb_3Sn cavity performance compared to the best Wuppertal Nb_3Sn cavity, from [105] along with SEM and TEM cross section and gap measurements from [103], copyright 2015 AIP Publishing LLC (d).

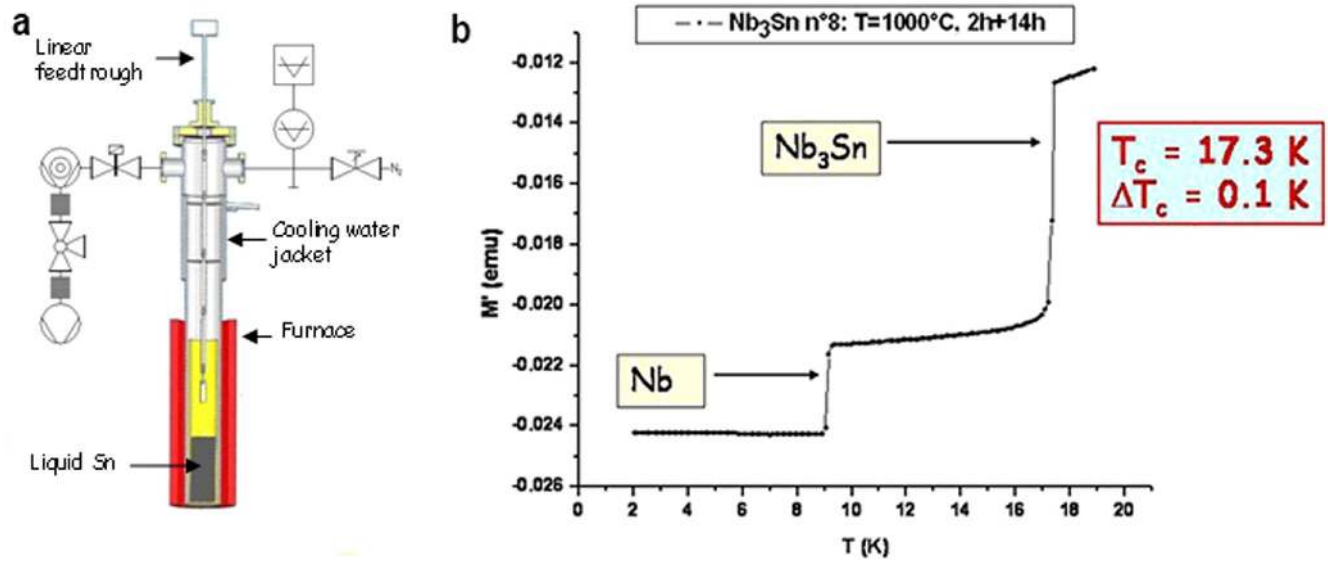

Figure 24. Hybrid liquid surface diffusion setup, courtesy of Deambrosis (a) and transition curve for Nb_3Sn produced by *hybrid liquid diffusion* [106], copyright 2006 Elsevier (b).

layer (10–20 μm) between two Cu layers [108]. The first Cu layer acts as a seed layer improving the adhesion of Sn on the substrate. The final Cu layer (10–15μm) acts as a barrier limiting Sn coalescence during thermal treatments. Good Nb_3Sn properties with T_c higher than 17 K are achieved. However a bronze (Sn–Cu) layer is formed on the top surface which would have to be removed if this technique is considered for SRF cavities. The advantage of these techniques would be the simplicity of the process at low temperatures, and ease of application to convoluted surfaces.

6.4. V_3Si

V_3Si is the first of the discovered A15 compound with $T_c = 17$ K at perfect stoichiometry (figure 25(a)). One of the rare A15 compounds to form congruently from the melt, it is a highly ordered compound with a stable A15 phase and a linearly increasing T_C in the range of 19–25 at% Si. A maximum T_C of 17.1 K and RRR values around 80 are obtained for a Si content of 25 at% (figure 25(b)) [5, 110] . Large single crystals can be grown over the whole A15 phase range by zone melting or by recrystallization at 1870 °C. However, one aspect to consider, in the case of SRF applications, is the large diffusion coefficient of V into Nb at high temperature. One needs then to consider a substrate other than bulk Nb or an interlayer that can be an effective barrier between V and the Nb substrate.

Magnetron sputtering [111], reactive sputtering [112] and co-sputtering [113] in a SiH_4 atmosphere have been used with

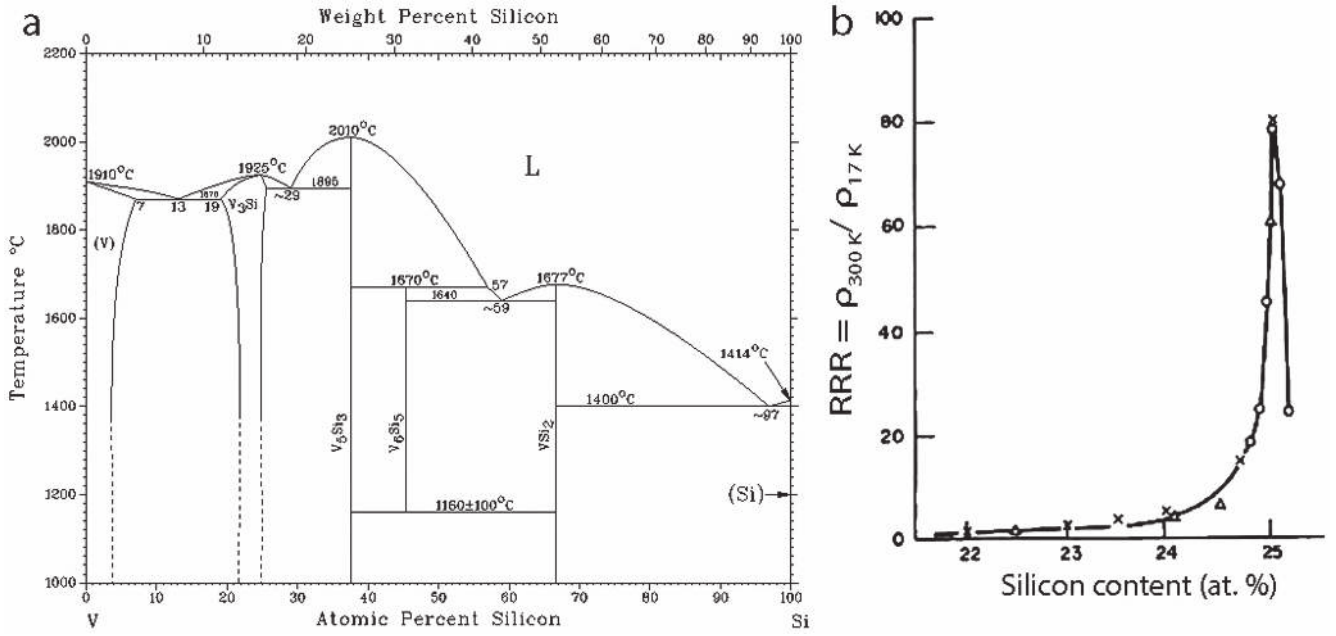

Figure 25. Phase diagram for the V–Si system [109], copyright 1995 Springer US (a); RRR curve for V_3Si versus Si content from [5] (b).

success to produce V_3Si films. The magnetron sputtered films displayed typically a T_c of 16.3 K ($T_c = 0.1$ K) and a resistivity of 3–5 $\mu\Omega$ cm. RF mesurements at 3.5 GHZ in a stripline resonator in [111] show an RF response for sputtered V_3Si films consistent with the weak coupling BCS theory predictions. the calculated R_{BCS} at 4.2 K and 3.5 GHz is lower than for bulk Nb. The Q-slope versus magnetic field was higher than for bulk Nb, yet lower than for NbTiN. The films produced by reactive sputtering showed a T_c of 16.2 K and RRR value of 16.7. Annealing has a positive effect on the sputtered films yielding T_c of about 17 K and a RRR around 18, no matter the initial film properties.

Another production method is silanization of V_3Si layers by silanization of V substrate and thermal diffusion [106, 114]. A V substrate (bulk or film) is first annealed in a silane (SiH_4) atmosphere. SiH_4 is decomposed and Si diffuses in the substrate. The sample is then annealed in vacuum to get rid of hydrogen. $T_c = 16.8$ K has been obtained with this technique [106]. Some attempts to deposit V_3Si on 6 GHz V cavities were done. Despite the good quality of the material produced on samples, the RF results have been inconclusive [115].

6.5. Mo_3Re

Outside the regime of V and Nb based A15 superconductors, Mo_3Re presents some potential for SRF applications. The solid solution is free from bulk and surface inhomogeneities. In contrast with Nb, the solubility of interstitials such as O is low. It is a strong coupling superconductor with low κ, reasonable H_{c1} (50 mT) but a small penetration depth λ. The bulk is in the tetragonal σ phase, with low T_c (figure 26(a)). Thin films typically exhibit a higher T_c than the bulk material [116]. High T_c (up to 15 K for a Re content ranging from 25 to 62 at%) has been reported in literature [116–118] outside the A15 stoichiometry, for $Mo_{60}Re_{40}$ films deposited at high temperature (>1000 °C). Films deposited at low temperature (300 °C) from a composite $Mo_{60}Re_{40}$ target yielded T_c values around 11 K [119]. The best Mo_3Re films were produced by dc magnetron deposition on α-Al_2O_3, Cu and Nb substrates maintained at 950 °C. The films are post-annealed at 800 °C–856 °C to increase the crystallinity (bcc phase) and the sharpness of the transition . $T_c = 12$ K has been obtained for $Mo_{60}Re_{40}$ composition. $T_c \sim 11.2$ K was obtained for $Mo_{75}Re_{25}$ (figure 26(b)) deposited at 680 °C without annealing.

The deposition of Mo_3Re by CED™ has been briefly investigated [121]. Transitions temperatures from 7 to 13 K were obtained. However, most of the best results were achieved for high substrate temperatures (700 °C–900 °C). Films close to stoichiometry ($Mo_{2.7}Re_1$) showed RRR of 6 with a T_c of about 11 K. The results were most likely hindered by the presence of Al and Mg impurities in the film. However, this exploratory work has not yet led to deposition on cavities.

7. Magnesium diboride

7.1. MgB_2 structure and superconductivity

The superconductivity of MgB_2 has been discovered in 2001 with $T_c = 39$ K [122]. MgB_2 has a hexagonal structure (figure 27(a)) with graphite-type boron (B) layers separated by hexagonal close-packed layers of magnesium (Mg) [123].

The superconductivity comes from the phonon-mediated Cooper pairs production similar to low-T_c superconductors except for the two-gap nature [124, 125] with $\Delta_p = 2.7$ meV and $\Delta_s = 6.7$ meV (see figure 27(b)).

The RF response has shown lower energy gap behavior. This lower gap is still about twice the gap of Nb (1.5 meV).

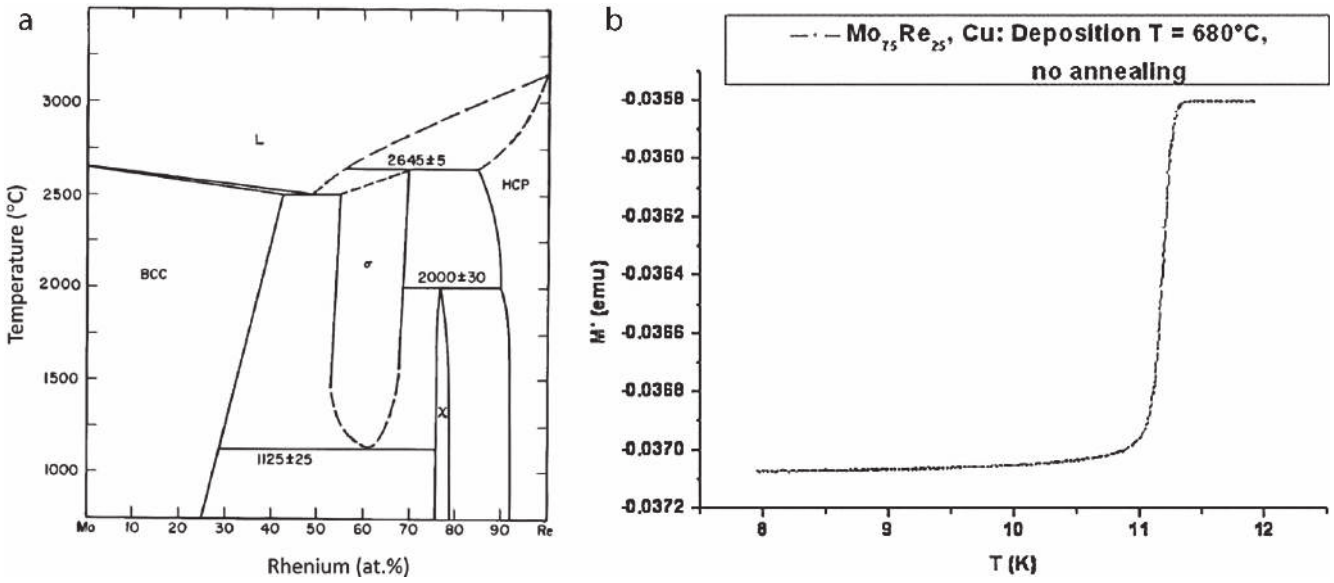

Figure 26. Phase diagram for the Mo–Re system from [120], copyright 1980 IAEA (a) and transition curve of an annealed sputtered $Mo_{75}Re_{25}$ deposited on copper from [106], copyright 2006 Elsevier (b).

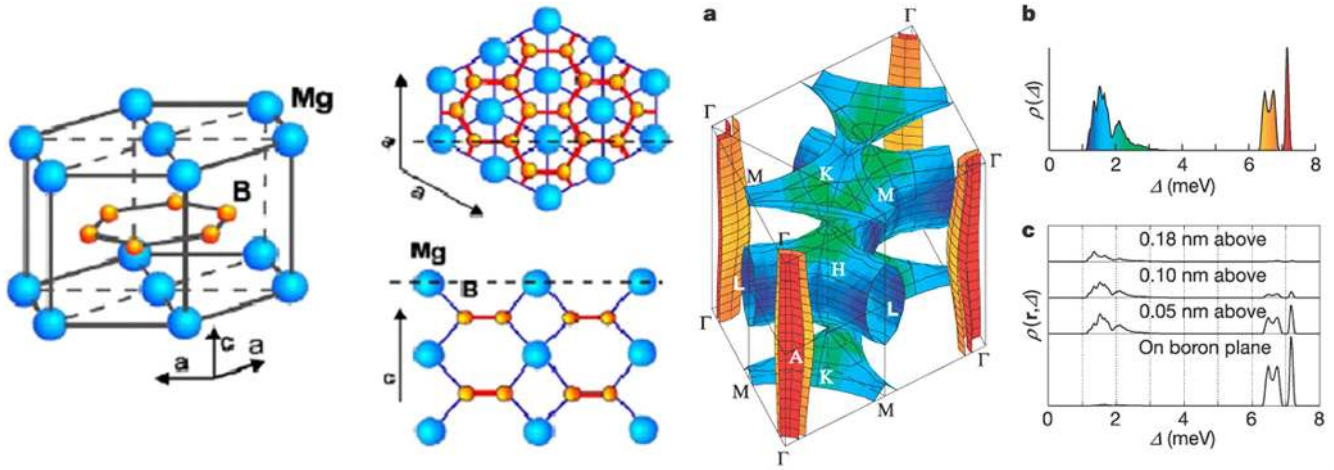

Figure 27. MgB_2 structure, adapted from [123], copyright 2001 IOP Publishing Inc. (a) and two-gap nature from [125], copyright 2002 Nature Publishing Group (b).

The normal resistivity can also be made quite low (best values are $\leqslant 1$ $\mu\Omega$ cm). With a higher T_c than Nb, a low resistivity, a larger gap, a higher critical field (see table 1), there appears to be room for better performance than Nb.

7.2. Film growth, properties and RF performance

Different techniques have been investigated to produce thin films of MgB_2 like pulsed laser deposition (PLD), low pressure CVD, molecular beam epitaxy (MBE), etc. However, MgB_2 thin films growth presents some challenges. A high pressure Mg vapor is needed for MgB_2 phase stability (figure 28). The material is susceptible to contamination with O and C. Thus, a reducing environment during coating is needed to avoid oxidation. The use of pure sources of B and Mg is also a requirement to produce good quality films.

The best results have been obtained with hybrid physical chemical vapor deposition (HPCVD) [127, 128] which combines physical and CVD. The system (see figure 29(a)) uses a quartz tube reactor and a susceptor inductively heated. H_2 is used as carrier gas at high flow (400 sccm–1 slm) and high pressure (100 Torr). Diborane, B_2H_6, is used as a high purity source of B. Pure bulk Mg is placed by the substrate on top of the susceptor. When the susceptor is heated up to 550 °C–760 °C, a high Mg pressure is generated in the vicinity of the substrate. The film growth is switched on and off when the precursor gas is switched on and off in the reactor. The HPCVD MgB_2 films have excellent structural and superconducting properties [127]. The high temperature used in HPCVD favors excellent epitaxy and crystallinity, yielding RRR values in excess of 80 (figures 29(b) and (c)). The generated surface is smooth (rms roughness <10 Å) with

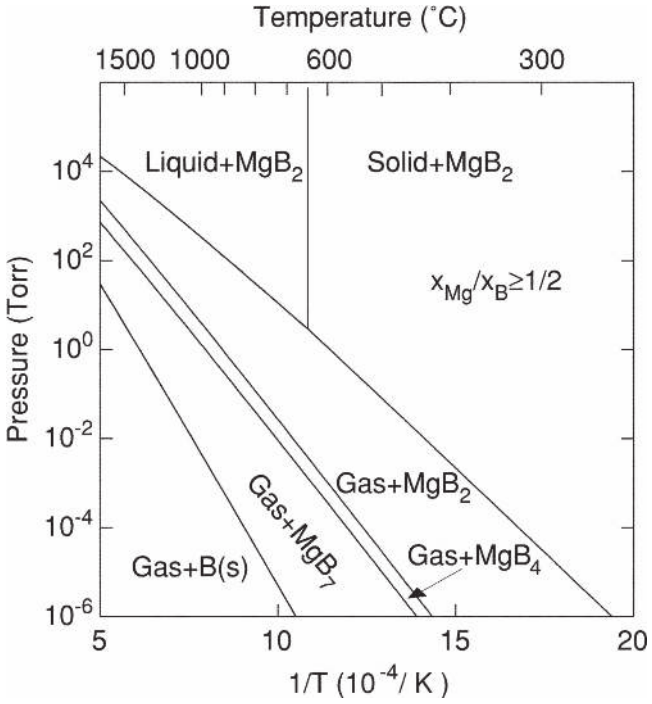

Figure 28. Mg–B phase diagram from [126], copyright 2001 AIP Publishing LLC.

well-connected grains and clean grain boundaries. The low resistivity (<0.1 $\mu\Omega$ cm with N_2 addition) and high T_c (~42 K due to tensile strain) promise a low R_{BCS}. The long coherence length ξ and short penetration depth λ promise high H_c (~820 mT). The films have good thermal conductivity (free from dendritic magnetic instability). The nonlinearity properties can be tuned by changing scattering in the two bands, with carbon doping for example.

HPCVD MgB_2 films have been deposited on various metal substrates like stainless steel, Nb, TiN and maintained good properties. The microwave performance at 10 GHz (figure 30(a)) of HPCVD films on 50 mm samples has been measured with Q-values around 10^4 at 20 K [129]. RF measurements performed at 7.5 GHz in a TE_{011} sapphire-loaded Nb cavity are represented in figure 30(b) were also performed [130]. Developments are currently on going on Cu and Nb substrates for cavity applications [131].

Good MgB_2 films can also be obtained by *in situ* reactive evaporation [132–134] where substrates are exposed to a high-pressure Mg vapor in a pocket heater for a controlled time, using a rotating mechanism. This technique present several advantages like a localized source of Mg vapor, a negligible amount of MgO in the pocket, B evaporation in vacuum, no need to control the Mg/B flux ratio, the ability to

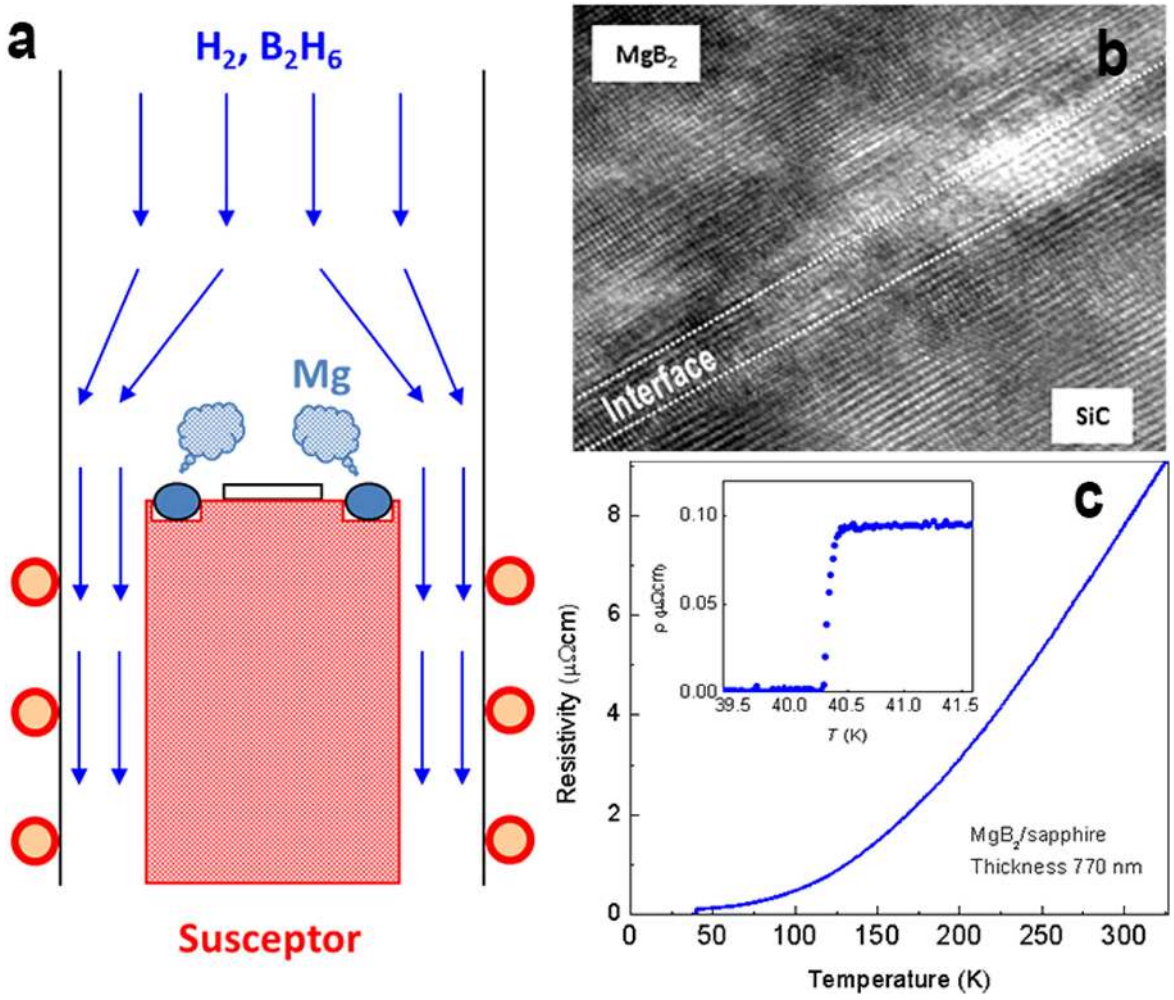

Figure 29. Schematic of the HPCVD system used in [127], copyright 2007 Elsevier (a); TEM cross-section (b), RRR curve (c) of MgB_2 films.

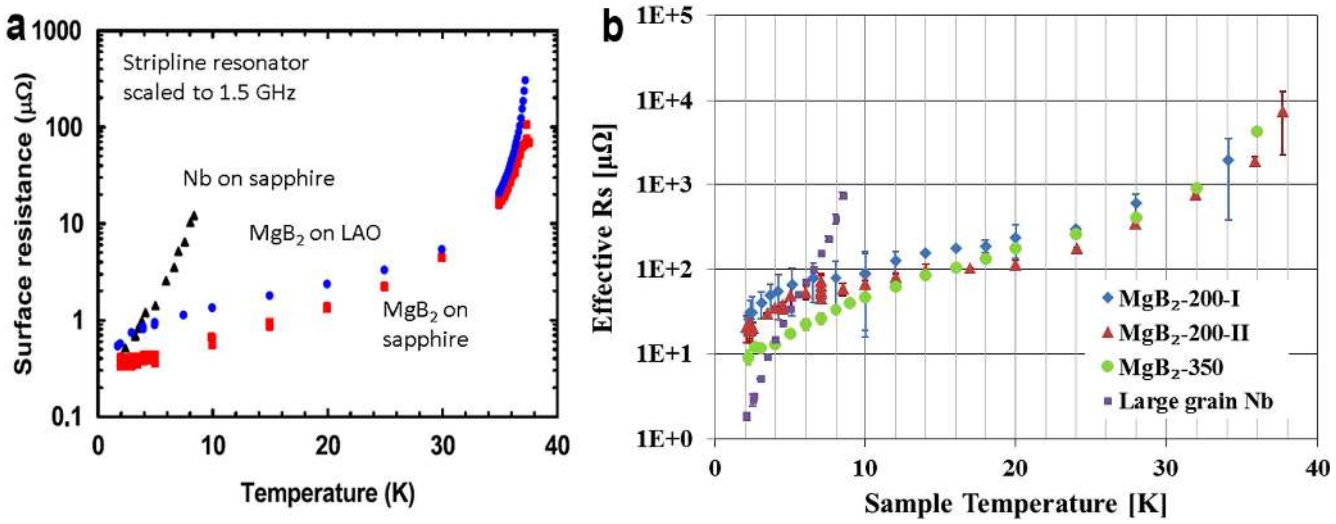

Figure 30. Surface resistance measurement at 2 GHz (scaled at 1.5 GHz) of HPCVD MgB_2 films deposited on α-Al_2O_3 and LaO [134](a); Effective surface resistance versus sample temperature of MgB_2 films on sapphire and of a large grain Nb sample, measured at 7.5 GHz (from [130], copyright 2012 IOP Publishing Inc.).

separate the substrate temperature from Mg temperature. Conceptually this system offers also the possibility to generate uniform growth on multiple and various large area substrates. The surface resistance of MgB_2 films produced was evaluated as a function of temperature and field at 10.7 GHz in a stripline and dielectric resonators. The results were very similar to the HPCVD MgB_2 films.

Good results have also been obtained with CVD [135]. The process could be easily transfered to cavity shape coating with a two steps process [136]: the cavity is first coated by CVD with a B layer at 400 °C–500 °C. The B layer is then reacted with Mg vapor to form MgB_2 at 850 °C–900 °C.

One of the challenges with using MgB_2 for SRF application is the degradation of the film properties with exposure to moisture (the resistance increases and T_c degrades). One way to overcome such degradation during the common cavity surface cleaning procedures may be to use a cap layer to protect the MgB_2 film.

8. Oxypnictides

8.1. Structure

Recently a new family of superconductors, the pnictides, has been discovered, accounting up to a few thousand compounds.

These materials are structured with the oxypnictide base (ReOMPn) where M = Fe, Co, Ni, Pn = As or P, Re = La, Nd, Sm, Pr (figure 31(a)). They are layered like HTS with T_c ranging from <10 to 55 K. The superconductivity occurs on the tetrahedrally coordinated FeAs layers with magnetic pair-breaking Fe^{2+} ions [138]. Superconductivity typically appears upon charge carrier (electron or hole) doping, and the undoped compound is characterized as metallic or semi-metallic. T_c is related to the structural parameters, in particular, with the height of the anion (As, P, …) from the Fe layer (figure 31(b)) [139, 140]. Tests in high magnetic fields suggest that the H_{c2} of $LaFeAsO_{0.89}F_{0.11}$ may be about 64 T. A different La-based material ($La_{0.8}K_{0.2}FeAsO0.8F_{0.2}$) tested at 6 K predicts H_{c2} up to 122 T. Numerous studies are ongoing to understand the intricate superconductivity mechanism in Fe-based superconductors. A detailed review of the different pnictide structures and their physical properties is given in [140].

For s-wave members of the pnictide family, Δ_{oxy} = 5–10 meV $> \Delta_{Nb_3Sn} = 3$ meV [141]. However, these compounds have a high ρ_n ($\sim$1 mΩ cm $\sim 10\rho_n^{MgB_2}$), a high value of λ (180–250 nm) and low H_{c1} ($\sim$10 mT). R_s for these materials can still be much lower than R_s of Nb_3Sn, but a structure based on SIS multilayers is necessary (refer to next section).

8.2. Film growth and properties

High quality epitaxial films have been grown via MBE, although only on a small scale (1 cm^2) [141–143]. Another commonly used deposition technique is PLD (pulse laser deposition) with post-annealing [144–146]. with this technique both epitaxial and polycrystalline films are deposited (figures 32(a) and (b)). The evaluation of such structures is ongoing in the framework of a collaboration between the University of Wisconsin (WS, USA) and Old Dominion University (VA, USA).

9. SIS multilayers

9.1. Theory

In the quest of improving the RF response of SRF cavities, an alternative concept was proposed, in 2006, by Gurevich [1] which would allow to take advantage of superconductors with

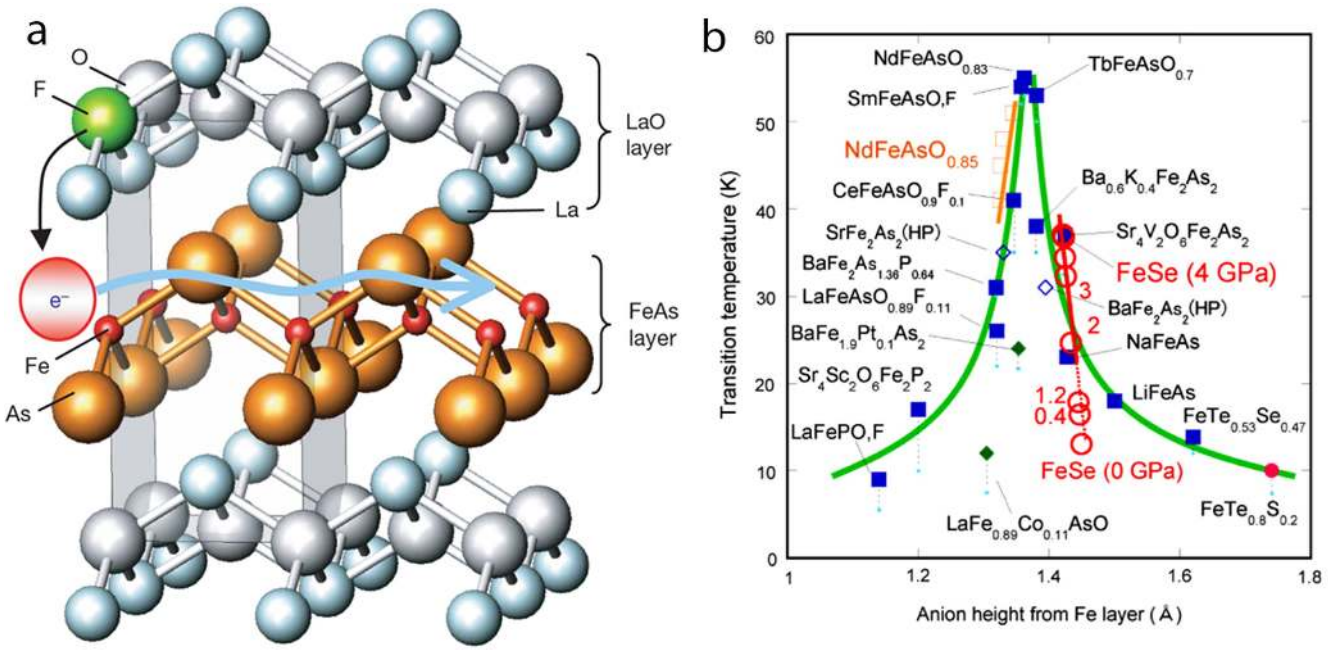

Figure 31. Oxypnictides structure from [137], copyright 2008 Nature Publishing Group (a); anion height dependence of T_c for Fe-based superconductors, from [139], copyright 2010 IOP Publishing Inc. (b).

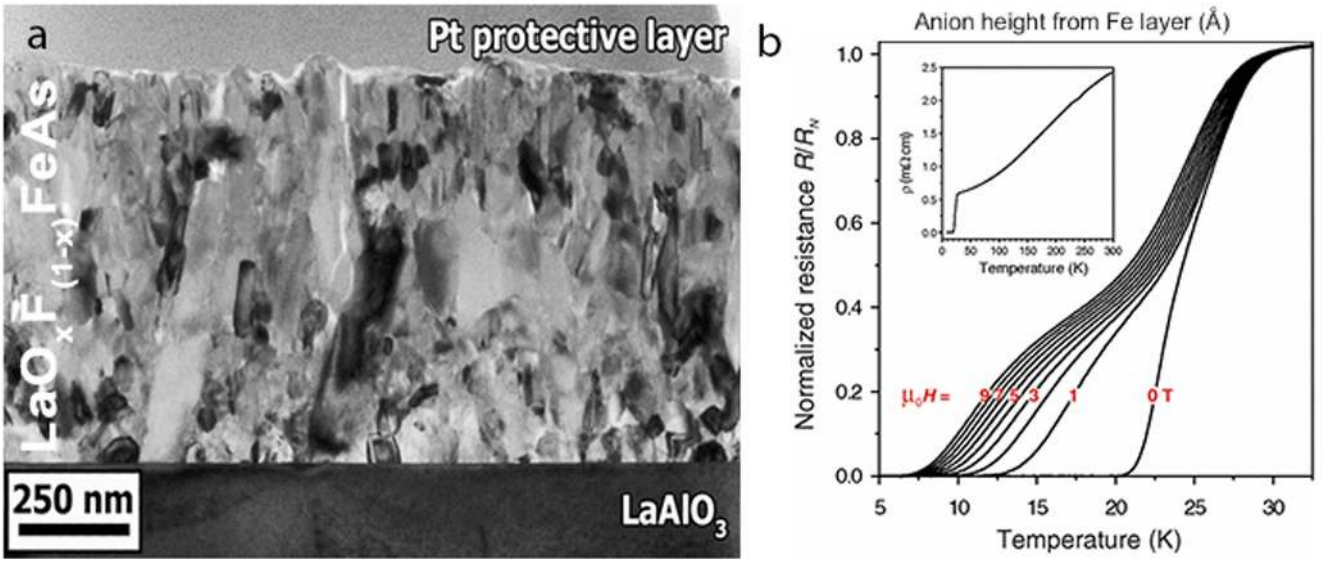

Figure 32. TEM cross-section of a $LaFeAsO_{1-x}F_x$ thin film (a) and its resistivity as a function of temperature (b), from [145], copyright 2010 The American Physical Society.

high T_c and high H_c without being penalized by their lower H_{c1}. The idea is to coat an SRF cavity (bulk Nb or thick Nb film) with a nanometric multilayer structure (SIS structures) composed of alternating superconducting (S) and insulating (I) layers with a thickness d_S smaller than the penetration depth λ_S.

If the superconducting film S is deposited with a thickness $d_S \ll \lambda_S$, the Meissner state can be retained at magnetic field much higher than bulk H_{c1} as

$$H_{fp}^{S} = \frac{2\phi_0}{\pi d^2}\ln\left(\frac{d}{1.07\xi_0}\right) \quad \text{for} \quad d \ll \lambda. \tag{17}$$

The strong increase of first flux penetration field H_{fp} in films, as shown in figure 33(a), allows the surface to support RF magnetic fields higher than the lower critical field H_{c1} of

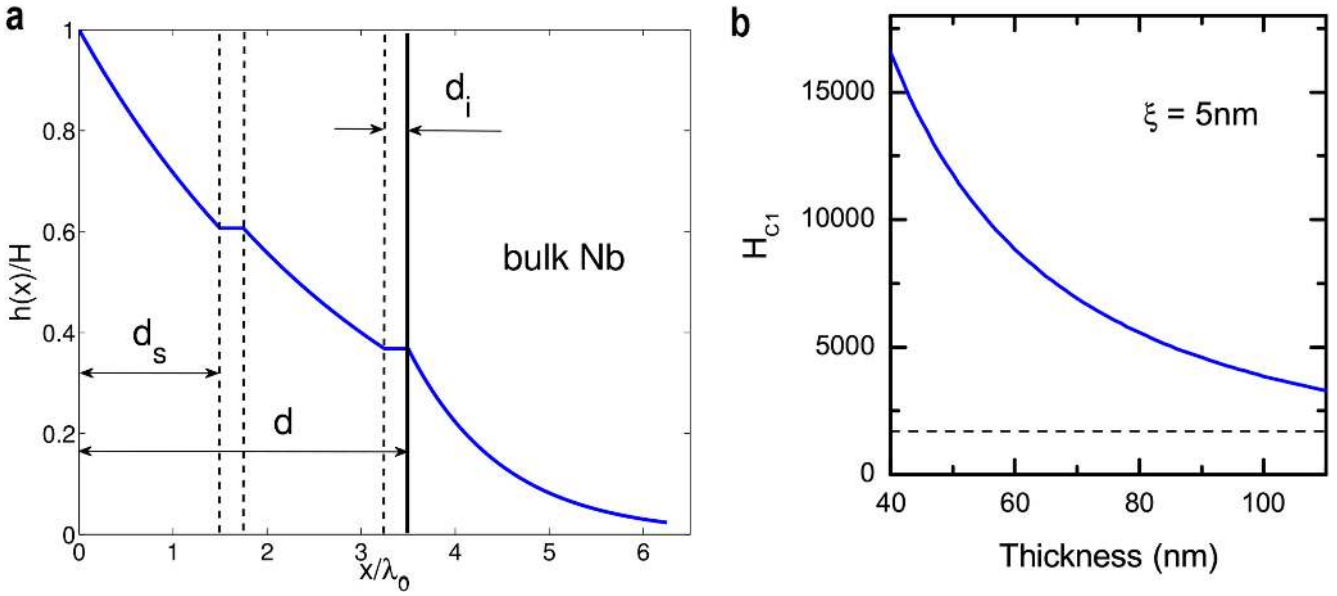

Figure 33. Distribution of the magnetic field h (x) in a SIS multilayer of total thickness d (a) from [147], copyright 2015 AIP Publishing LLC; enhancement of flux penetration field $H_{\rm fp}$ (or effective $H_{\rm c1}$) as a function of thickness for a superconducting thin film with a coherence length ξ of 5 nm. The dashed line corresponds to $H_{\rm c1}^{\rm Nb} = 170$ mT (b).

bulk Nb (figure 33(b)). The role of the thin insulating layer I is to inhibit vortex oscillations and prevent global vortex penetration in the cavity. Its thickness, $d_{\rm I}$, needs to be big enough to avoid Josephson junction effects. The BCS resistance is also strongly reduced because of the use of superconductors with a higher gap Δ (Nb_3Sn, NbTiN …). The effect can be furthered by adding SI layer sequences. The optimum number of SI layers is determined by a compromise between vortex dissipation reduction and superconductivity suppression at the S–I interfaces.

With such optimized SIS structures, Q-values at 4.2 K of two orders of magnitude above Nb values could be achieved, and the sustainable external magnetic field could be more than doubled.

Some refinements have been recently introduced [147–149] in order to accurately understand the field limit in the multilayered SIS structure. The Maxwell equations and the London equations were solved simultaneously with appropriate boundary conditions in order to derive the magnetic field electromagnetic field in the complete multilayered structure (S/I/substrate). The magnetic field distribution (and thus the screening current distribution $J \propto {\rm d}B/{\rm d}x$) in the S layer is different from the exponential decay $B = B_0 {\rm e}^{-x/\lambda_{\rm I}}$ (figure 34). When $d_{\rm S}$ and $d_{\rm I}$ are thin enough and $\lambda_{\rm S} > \lambda_{\rm substrate}^{\rm bulk}$, the screening current in the superconductor S layer is suppressed, and the surface field can exceed the superheating field $H_{\rm sh}^{\rm S}$ of the S layer. However, an extremely thin superconductor layer can not completely shield the underlying Nb substrate. Thus, there is an optimum thickness where the S layer is thin enough to significantly decay the magnetic field but still thick enough to protect the Nb substrate.

A description of the maximum field and optimum S layer thickness [147, 149], including the effects of an insulator layer with finite thickness, is derived by using the superheating field of the quasi-classical theory and is thus valid at $T \ll T_{\rm c}$. If the material properties are known, contour plots of the SIS structure maximum sustainable field can be produced as function of superconducting and insulating layer thicknesses, d_S and $d_{\rm I}$, as represented in figures 35(a) and (b). For example, for Nb_3Sn/I/bulk Nb structure, assuming $H_{\rm substrate}^{\rm Nb} = 170$ mT, $\lambda_{\rm substrate}^{\rm Nb} = 40$ nm, $H_{\rm c}^{\rm Nb_3Sn} = 540$ mT and $\lambda_{\rm S}^{\rm Nb_3Sn} = 120$ nm, the maximum field sustainable without vortex penetration would be 350 mT. The optimum layer thicknesses would be $d_{\rm S}^{\rm Nb_3Sn} \sim 170$ nm and $d_{\rm I} \sim 10$–20 nm (figure 35(a)).

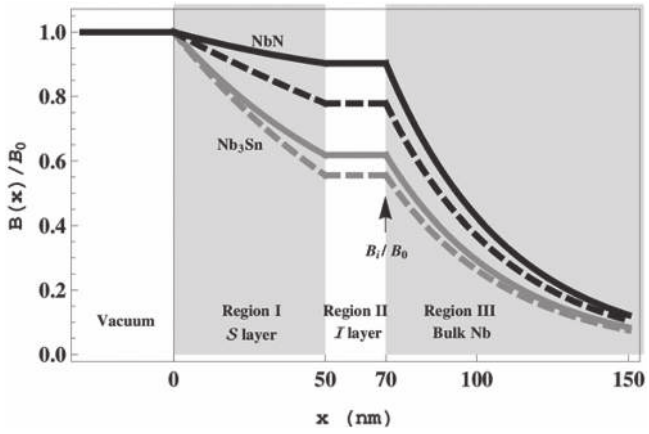

Figure 34. Examples of magnetic field attenuations in a typical multilayered structure for NbN and Nb_3Sn, from [148], copyright 2014 AIP Publishing LLC.

Thus far, the models do not take into account dielectric losses in the insulating layer I or any perpendicular component in the applied magnetic fields. The theoretical concepts assume ideal superconducting and insulating materials. In real

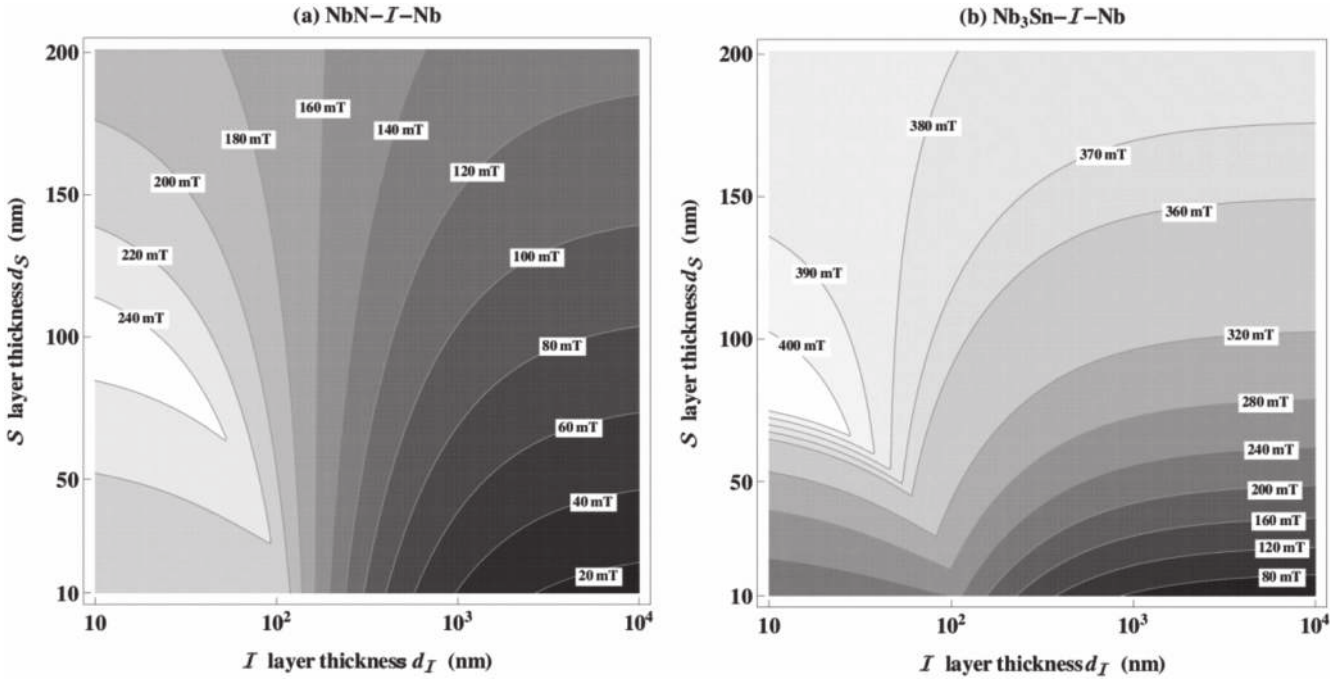

Figure 35. Contour plots for maximum achievable peak surface field without vortex dissipation, as function of superconducting (S) and insulating (I) layers thickness, for NbN (a) and Nb_3Sn (b) structures on an ideal Nb surface ($\lambda = 40$ nm, $B^{bulk} = 200$ mT), from [148], copyright 2015 AIP Publishing LLC.

SIS structures, both type of layers, S and I, present defects, most likely a non-negligible surface roughness, and some non-uniformity in thickness. The superheating field in the S layer is then suppressed due to enhancement of the screening current. This can be taken into account in calculations by introducing a material *suppression factor* η, which is dependent on the size and aspect ratio of the defect, the coherence length of the material ($\eta \sim 0.85$ for a typical electropolished Nb surface) [149]. The superheating field of the SIS structure and the optimal S layer thickness can be determined if surface topographical data is available. If one takes the Nb_3Sn/I/bulk Nb example mentioned above and assumes a suppression factor $\eta \sim 0.7$, the maximum field sustainable without vortex penetration becomes 350 mT with an optimum layer thickness $d_S^{Nb_3Sn} \sim 130$ nm. Although materials with higher superheating field H_{sh}, such as Nb_3Sn, MgB_2, would produce a more significant RF field performance enhancement, SIS multilayers based on '*dirty*' or '*doped*' Nb can increase the maximum field sustainable but also benefit from a significant Q improvement [3, 4].

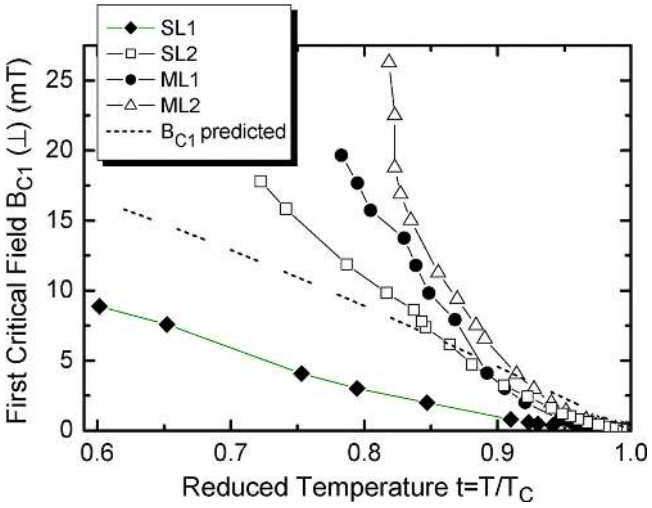

Figure 36. Third harmonic results for single and multilayer Nb/Al_2O_3 films measured at INFN-Napoli, from [58], copyright 2009 IEEE.

9.2. Ongoing research

Since the past few years, several efforts towards experimental demonstration of the Gurevich concept have been ongoing in various institutions using different superconducting and insulating materials for SI layers.

9.2.1. SIS based on Nb films and Al_2O_3. At INFN Roma and Napoli (Italy), alternating 80 nm layers of Nb and Al_2O_3 were deposited on 250 nm thick Nb film substrates via dc and RF magnetron sputtering [58]. The film response was studied using inductive third-harmonic measurements (described in details in [150]), in which a 1kHz magnetic field is applied by a *pancake coil* to small flat multilayer samples. The third-harmonic voltage responses induced by vortex motion in the film is then detected by the same coil. These measurements indicate a clear improvement in effective B_{c1} due to multilayer coatings, as shown in figure 36. The first critical field of multilayer films produced by magnetron sputtering shows a temperature dependence substantially better than the one reported for the thick Nb film (SL2). The dashed line on the

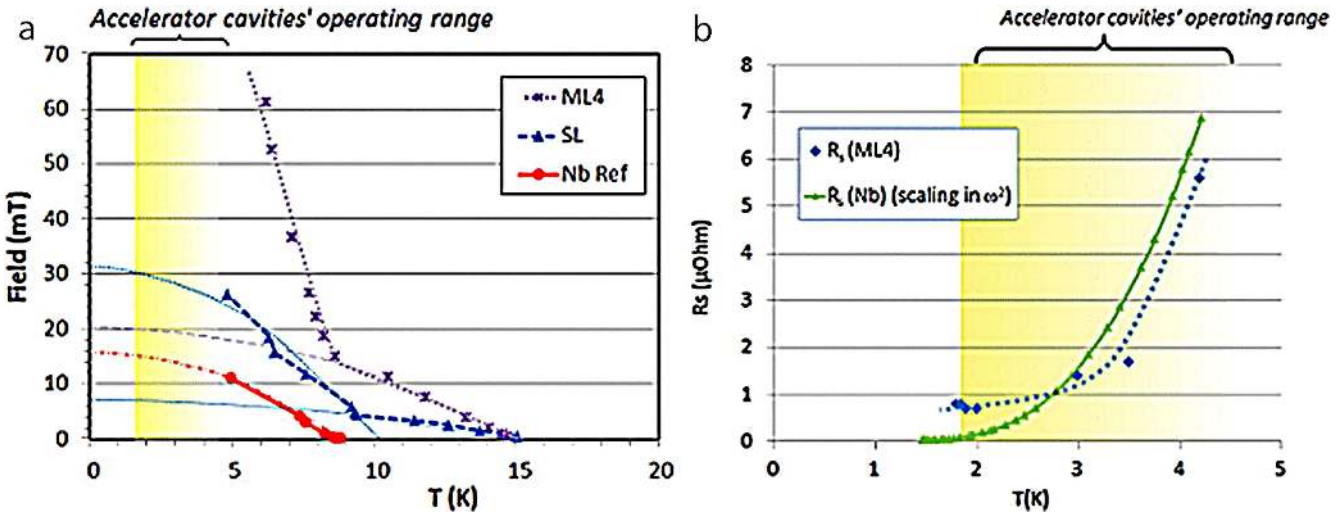

Figure 37. Third harmonic signals in a modified SQUID magnetometer for a reference Nb film/MgO and Nb/MgO/Nb SIS structures (a); Surface resistance of a $(NbN/MgO)_4/Nb$ structure determined by calorimetric method at $B = 1$mT (b), from [154], copyright 2013 AIP Publishing LLC.

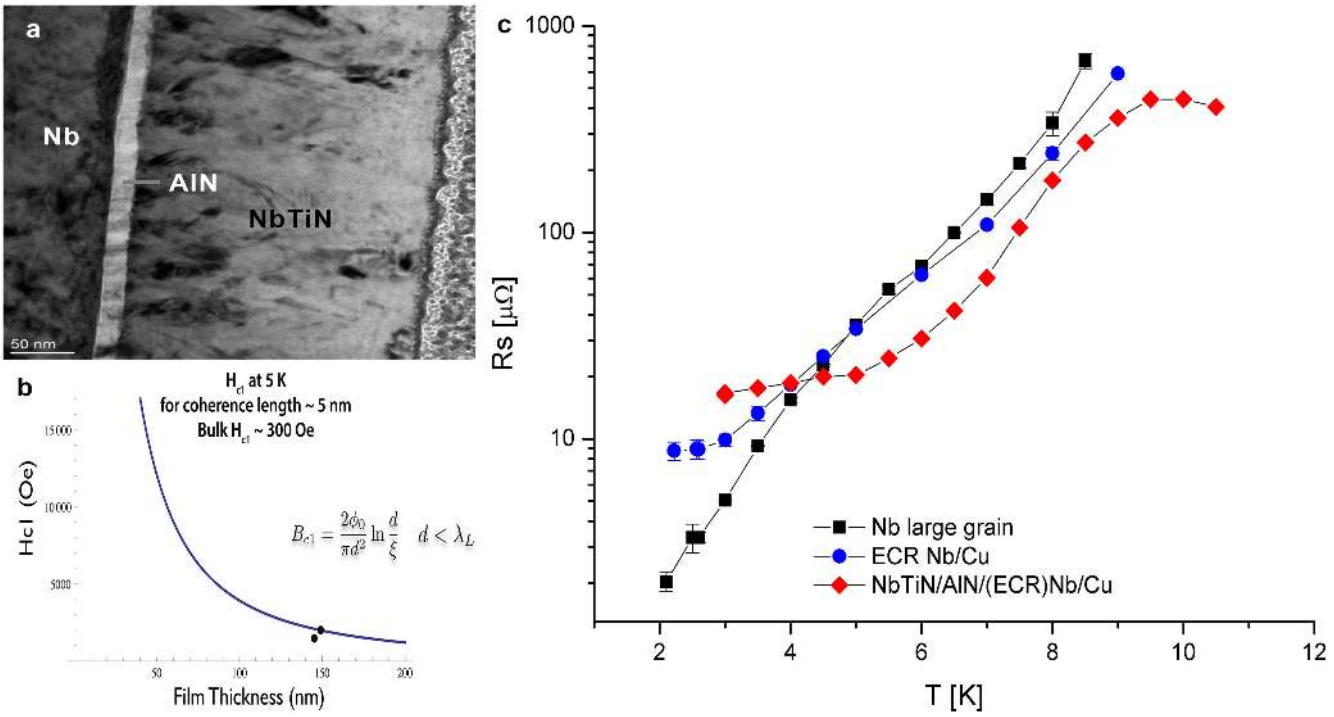

Figure 38. TEM cross-section (a) and first flux penetration (b) for NbTiN/AlN structures; RF measurement at 7.5 GHz of a NbTiN/AlN/Nb/Cu structure compared with the original Nb/Cu film and large grain bulk Nb (c) [156].

graph refers to the predicted first critical field temperature behavior by taking $\lambda(0) = 100$ nm and a ratio $\lambda/\xi = 2.5$ fairly constant in temperature. Both multilayered structures, ML1 and ML2, show a field temperature dependence substantially better than for the single layer Nb film (SL2), with the highest value measured for the structure with double SI layers (ML2). This is was the first experimental result in agreement with the concept proposed by Gurevich [1]).

9.2.2. SIS based on NbN and MgO. Encouraging results have also been achieved with SQUID magnetometry measurements on SIS multilayer structures based on NbN (S) and MgO (I) at CEA Saclay [151, 152] and The College William & Mary [153].

In the work conducted at Saclay [151, 152, 154], 25 nm layers of NbN (superconductor) and MgO (insulator) were deposited on 250 nm thick Nb film substrates via magnetron sputtering. The dc magnetization response of the samples was studied using SQUID and local magnetometry (figure 37(a)). The first penetration fields for the reference Nb film sample, for the single NbN/MgO nanolayer sample (SL) and for the 4 period multilayers (ML4) were determined with the third

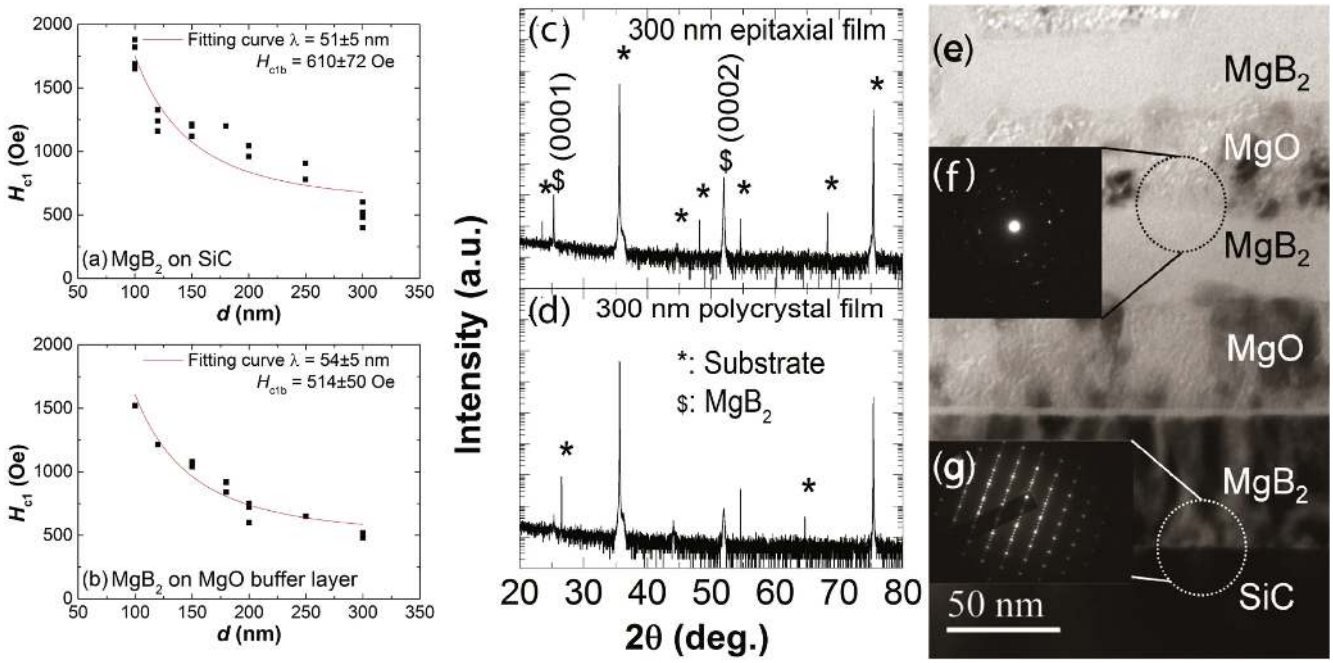

Figure 39. Measured H_{C1} (4 K) as a function of thickness for hetero-epitaxial (a) and polycrystalline (b) MgB_2 films; associated XRD spectra (c), (d) and TEM cross-section (e)–(g); from [158], copyright 2015 AIP Publishing LLC.

harmonic local probe. One can note that, around 6 K, the first penetration of vortices in the SL structure appears at a field value about twice the reference one, while the 4 layer sample (ML4) is about 10 times higher. RF surface measurement (in a TE_{011} cavity, figure 37(b)) of a NbN/MgO/Nb structure show a multilayer resistance $<1\ \mu\Omega$, lower than that of bulk Nb.

9.2.3. SIS based on NbTiN and AlN. Another material of interest for SIS structures is NbTiN, which is under study at Jefferson Lab [65]. Here, NbTiN and AlN films are deposited by reactive magnetron sputtering at 450 °C with good microstructure as shown in the TEM cross-section in figure 38(a). Flux penetration field measurements by SQUID magnetometry (figure 38(b)) as described in [153] were performed on 150 nm thick NbTiN films deposited simultaneously on MgO and AlN ceramic. The sample deposited on MgO with a T_c corresponding to the δ-phase demonstrated a first flux penetration field enhancement up to 200 mT from 30 mT as measured for a 2 μm bulk-like NbTiN/MgO. The sample deposited on the rough AlN ceramic, despite a T_c representative of the γ-phase, still shows a first flux penetration field enhancement up to 135 mT. The thickness of these films is about 150 nm which is still very close to the NbTiN penetration depth. Thickness studies are under way to determine the optimum for flux penetration field H_{fp} enhancement. In this case, the insulator of choice is AlN as it is reported in the literature [155] that an AlN buffer layer enhances the properties of NbTiN (increase of T_c).

The RF response of such an SIS structure was measured on a 50 mm disk sample in a 7.5 GHz sapphire loaded TE_{011} cavity. Figure 38(c) shows the surface resistance measurement of an NbTiN/AlN structure coated on a thick Nb film. The performance of a large grain Nb reference sample and the initial performance of the ECR Nb/Cu film are also represented for comparison. The film used as a substrate was coated *ex situ* by energetic condensation [156]. The SI structure was deposited at 450 °C *in situ* after a 24 hour-bake at 450 °C. The sample was then annealed at 450 °C for 4 hours. The microstructure of the SI layers is shown in the associated TEM cross-section (figure 38(a)). The multilayer structure shows an increase of surface resistance below 4 K most likely due to the reduction and diffusion of the Nb film oxide layer into the film bulk. However, above 4 K, the surface resistance of the SIS structure is lower than for the initial ECR Nb film and than for bulk Nb.

9.2.4. SIS based on MgB_2 and MgO. First flux penetration measurements were performed for MgB_2 films of different thicknesses (figures 39(c)–(g)) and deposited via the HPCVD method mentioned in section 7.2 [157, 158]. Some of the results are represented in figures 39(a) and (b) (from [158]) along with expected theoretical curves for first flux penetration field enhancement for particular coherence lengths (solid lines). Associated error for critical field measurements are on the order of ~100 Oe and not represented. The experimental data follow well the theoretical curve.

The preliminary results achieved in the studies described above give interesting indications on the efficacy of multi-layer films in postponing the onset of flux penetration. Note, however, that most of these studies are conducted at dc or at very low (kHz) frequencies, complicating any potential cavity predictions concerning RF surface resistance. Efforts are currently on-going to create such SIS structures on bigger samples (for example, for measurements on quadrupole

resonator cavities, [66]) and in cavity structures to fully establish the potential of this concept.

Thin film deposition via CVD, PVD or atomic layer deposition (ALD) techniques is the most likely route to be chosen for implementation of SIS multilayer structures. It is well known that film quality is highly dependent on the particular material deposited, the underlying substrate nature and quality, the chosen deposition technique(s)…. For example, the lattice mismatch between the I layer and the substrate, the S and I layers influence the intrinsic strain in the different layers. The superconducting parameters (penetration depth λ, mean free path l, coherence length ξ…) of the S layers and RF performance (R_s), maximum sustainable field H_{fp} of the final SIS structure are highly dependent on the quality of the alternating films. Also, the growth conditions for an optimum SIS structure will most likely be a compromise between the optimum growth for individual S and I layers. One of the critical practical aspects is that the chosen technique needs to allow successive deposition of each layer at a temperature low enough to prevent intermixing of the alternating layers.

10. Conclusions

Over the years, some attempts have been made to study alternatives to bulk Nb for SRF applications. There is re-gained interest to develop *bulk-like* Nb films with energetic condensation techniques which produce unprecedented film quality. Most of the samples or cavities prepared for SRF applications using alternative materials have been produced by reactive magnetron sputtering or thermal diffusion. Revisiting the production of alternative materials with energetic condensation techniques such as vacuum arc deposition, energetic deposition by ECR plasma, or techniques like ALD could be a route to explore these alternative materials under a new light. For example, vacuum arc and ECR plasma deposition produce very dense films with nm-scale roughness. Attempts to coat other SRF materials such as NbN, Nb_3Sn, Mo_3Re with vacuum arc deposition have been made at INFN-Rome but the results are, so far, non-conclusive. Most of the measurements to qualify materials for SRF applications, so far, consist mainly in T_c and resistivity characterization, with seldom RF characterization at useful frequencies. Direct comparison of the RF performance with bulk Nb is needed for a more systematic and extensive investigation of Nb thin films and alternative materials. The measurements of H_{fp}, H_{c1}, H_{c2}, and other superconducting parameters in useful conditions and the influence of the material composition and properties on these parameters would be most useful. The multilayer approach opens the door to further potential improvement for SRF cavities, taking benefits from the advantages of higher-T_c superconductors without the limitation of H_{c1} or H_{sh}. The development of Nb films and other superconducting materials for SRF cavities application has yet to show the full potential of these alternatives to bulk Nb, due to overall relatively modest research efforts. Today's exceptional performance of bulk Nb SRF cavities is the fruit of five decades of significant research and funding efforts. *Second generation* Nb films, Nb_3Sn thick films and multilayer SIS structures are now showing glimpses of potentially achievable high field RF performance while reducing the operation cost of accelerators. In order for these technologies to mature and fulfill their promises for future superconducting accelerators, considerable research and development efforts need to be invested.

Acknowledgments

This material is based upon work supported by the US Department of Energy, Office of Science, Office of Nuclear Physics under contract DE-AC05-06OR23177. The author would like to thank for fruitful discussions and for sharing data and information, over the years, G Eremeev, L Phillips and C Reece (JLab, USA), C Antoine (CEA Saclay, France), A Anders (LBNL, USA), S Aull, C Benvenuti and S Calatroni (CERN, Switzerland), V Palmieri, A Rossi and S Deambrosis (INFN-LNL, Italy), X Xi (Temple University, USA), T Tajima (LANL, USA), T Proslier, J Norem, and J Elam (ANL, USA), T Kubo (KEK, Japan), S Posen (FNAL, USA), A Gurevich (ODU, USA), R Russo (CNR-Napoli, Italy), RA Lukaszew (College William & Mary, USA).

References

[1] Gurevich A 2006 *Appl. Phys. Lett.* **88** 012511
[2] Dhakal P *et al* 2013 *Phys. Rev. Spec. Top. Accel. Beams* **16** 042001
[3] Grassellino A *et al* 2013 *Supercond. Sci. Technol.* **26** 102001
[4] Ciovati G, Dakhal P and Gurevich A 2014 *Appl. Phys. Lett.* **104** 092601
[5] Palmieri V 2001 *10th Workshop on RF Superconductivity Proc. (Tsukuba, Noguchi)* p 162
[6] Bardeen J, Cooper L and Schrieffer J 1957 *Phys. Rev.* **108** 1175
[7] Padamsee H, Knoblock J and Hays T 1998 *RF Superconductivity for Accelerators* (New York: Wiley) pp 58–102, 315–28
[8] Nam S 1967 *Phys. Rev.* **156** 487
[9] Mattis D and Bardeen J 1958 *Phys. Rev.* **111** 412
[10] Yogi T, Dick G and Mercereau J 1977 *Phys. Rev. Lett.* **39** 826–9
[11] Posen S, Valles N and Liepe M 2015 *Phys. Rev. Lett.* **115** 047001
[12] Matricon J and Saint-James D 1967 *Phys. Lett.* A **24** 241–2
[13] Ray P J Own work CC BY-SA 4.0, https://commons.wikimedia.org/w/index.php?curid=46193149
[14] Benvenuti C *et al* 1999 *Physica* C **316** 153
[15] Weingarten W 1995 *Proc. 7th Workshop on RF Superconductivity (Gif-sur-Yevette, France)* p 129
[16] Wang T *et al* 2001 *Proc. 10th Workshop on RF Superconductivity (KEK, Tsukuba, Japan)* p 264
[17] Durand C, Bosland P and Mayer J 1995 *IEEE Trans. on Appl. Supercond.* **5** 1107
[18] Benvenuti C *et al* 1991 *Proc. IEEE Part. Accelerat. Conf. (San Francisco)* vol. 2 (New York, USA: IEEE) pp 1023–5
[19] Benvenuti C, Circelli N and Hauer M 1984 *Appl. Phys. Lett.* **45** 583–4
[20] Calatroni S 2006 *Physica* C **441** 95–101

[21] Padamsee H 2009 *RF Superconductivity: Volume II: Science, Technology and Applications* (Weinheim: Wiley-VCH)
[22] Benvenuti C *et al* 2001 *Physica* C **351** 421–8
[23] Xiao B and Reece C E 2014 A new rst-principles calculation of eld-dependent RF surface impedanceof BCS superconductor and application to SRF cavities arXiv:1404.2523
[24] Bisoffi G *et al* 2007 *Proc. 13th Workshop on RF Superconductivity (Peking University, Beijing, China)* MO404 55
[25] Porcellato A-M 1996 *Nucl. Instrum. Methods* A **382** 121
[26] Sublet A *et al* 2013 *Proc. SRF13 (Paris, France)* TUP073 611, TUP076 620, TUP077 623
[27] Sublet A *et al* 2014 *Proc. IPAC 2014 (Dresden, Germany)* WEPRI042 2571
[28] Halbritter J 1995 *J. Supercond.* **8** 691
[29] Halbritter J 1992 *J. Appl. Phys.* **71** 339–43
[30] Kulik I and Palmieri V 1998 *Part. Accel.* **60** 257
[31] Singer W *et al* 2001 *Proc. 10th Workshop on RF Superconductivity (KEK, Tsukuba, Japan)* FA009 170
[32] Ribeaudeau M 1999 Elaboration et caractérisation de films de niobium déposés sur cuivre. Détermination de la résistance de surface de supraconducteurs par thermométrie sous vide *PhD Dissertation* Paris VI, France
[33] Arbet-Engels V *et al* 2001 *Nucl. Instrum. Methods Phys. Res.* A **463** 1–8
[34] Benvenuti C *et al* 2001 *Physica* C **351** 429–37
[35] Benvenuti C *et al* 2001 *Physica* C **361** 31–9
[36] Benvenuti C *et al* 2001 *Proc. 10th Workshop on Superconductivity (Tsukuba, Japan)* ed S Noguchi p 252
[37] Calatroni S *et al* 2003 Progress of Nb/Cu technology with 1.5 GHz cavities *Technical Report* No. CERN-TS-2004-002-MME (https://cds.cern.ch/record/791841/files/ts-2004-002.pdf)
[38] Halbritter J 1999 *Supercond. Sci. Technol.* **12** 883
[39] Palmer F 1988 *Proc. 3th Workshop on RF Superconductivity (Argonne, USA)* ANL- PHY-88-1 309
[40] Malev M and Weisser D 1995 *NIM Phys. Res.* A **364** 409
[41] Halbritter J 2001 *Proc. 10th Workshop on RF Superconductivity (KEK, Tsukuba, Japan)* p 292
[42] Colligon J S 1995 *J. Vac Sci. Technol.* A **13** 1649
[43] Sarakinos K, Alami J and Konstantinidis S 2010 *Surf. Coat. Technol.* **204** 1661–84
[44] Monteiro O R 2001 *Annual Rev. Mat. Sci.* **31** 111–37
[45] Anders A 2010 *Thin Solid Films* **518** 4087–90
[46] Brice D K, Tsao J Y and Picraux S T 1989 *Nucl. Instrum. Methods Phys. Res.* B **44** 68
[47] Eckstein W 1991 *Computer Simulation of Ion-Solid Interactions* (Berlin: Springer)
[48] Bilek M M M and McKenzie D R 2006 *Surf. Coat. Technol.* **200** 4345
Carter G 2000 *Phys. Rev.* B **62** 8376
[49] Hultman L and Sundgren J E 2001 *Handbook of Hard Coatings* ed R F Bunshah (Park Ridge, NY: Noyes) p 108
[50] Brown I G 1994 *Rev. Sci. Instrum.* **65** 3061
[51] Krishnan M *et al* 2011 *Supercond. Sci. Technol.* **24** 115002
[52] Wu G *et al* 2005 *Thin Solid Films* **489** 56–62
[53] Purandare Y P *et al* 2008 *J. Vac Sci. Technol.* A **26** 288
[54] Anders A 2008 *Cathodic Arc Sources.: From Fractal Spots to Energetic Condensation* (New York: Springer) pp 227–63, 363-407
[55] Anders A 2010 Unfiltered and filtered cathodic arc deposition *Handbook of Deposition Technologies for Films and Coatings* ed P M Martin and W Andrew 3rd edn (Netherlands: Amsterdam) p 466531
[56] Anders A 2002 *Appl. Phys. Lett.* **80** 1100–2
[57] Russo R *et al* 2005 *Supercond. Sci. Technol.* **18** L41
[58] Russo R *et al* 2009 *IEEE Trans. Appl. Supercond.* **19** 1394–8
[59] Langner J *et al* 2006 *Vacuum* **80** 1288–93
[60] Russo R 2001 *Proc. 10th Workshop on RF Superconductivity (Tsukuba, Japan)* 44 TL012
[61] Russo R *et al* 2007 *Proc. 13th Workshop on RF Superconductivity (Peking Univeristy, Beijin, China)* WE101 675
[62] Zhao X *et al* 2009 *J. Vac Sci. Technol.* A **27** 620
[63] Krishnan M *et al* 2012 *Phys. Rev. Spec. Top. Accel. Beams* **15** 032001
[64] Krishnan M *et al* 2013 *Proc. 16th Int. Conf. on RF Superconductivity (Paris, France)* WEIOA02 761
[65] Valente-Feliciano A-M 2014 Development of SRF thin film materials for monolayer/multilayer approach to increase the performance of SRF accelerating structures beyond bulk Nb *PhD Dissertation* Université Paris XI
[66] Aull S *et al* 2015 *Proc. 17th Int. Conf. on RF Superconductivity (Whistler, BC, Canada, 13–18 September)* TUBA03 494
[67] Horwat D and Anders A 2010 *J. Appl. Phys.* **108** 123306
[68] Anders A 2011 *Surf. Coat. Technol.* **205** S1–9
[69] Andersson J and Anders A 2012 *J. Appl. Phys.* **111** 053304
[70] Anders A 2009 *Phys. Rev. Lett.* **102** 045003
[71] Anders A *et al* 2011 *Proc. 15th Int. Conf. on RF Superconductivity (Chicago, USA)* TUIOA06 302
[72] Anders A 2004 *Appl. Phys. Lett.* **85** 6137
[73] Anders A and Mendelsberg R 2012 private communication
Rauch A *et al* 2012 *J. Appl. Phys.* **111** 083302
[74] Terenziani G, Calatroni S and Ehiasarian A P 2013 *4th Int. Conf. on Fundamentals and Industrial Applications of HIPIMS*
[75] Terenziani G *et al* 2013 *Proc. 16th Int. Conf. on RF Superconductivity (Paris, France, September 2013)* TUP078 627
[76] Vonsovsky S V, Izyumov Yu A and Kumaev E Z 1982 *Superconductivity of Transition Metals, their Alloys and Compounds* (Berlin: Springer) pp 259–68
[77] www.geocities.jp/ohba_lab_ob_page/structure6.html
[78] Brauer G 1960 *J. Less-Common Metals* **2** 131
[79] Guard R W, Savage J W and Swarthout D G 1967 *Trans. Metall. Soc. ATME* **239** 643
[80] Toth L 1971 *Transition Metal Carbides and Nitrides* (New York: Academic) ch 7
[81] Fabbricatore P *et al* 1989 *J. Appl. Phys.* **66** 5944
[82] Pham Tu M *et al* 1988 *J. Appl. Phys.* **63** 4586
[83] Benvenuti C *et al* 1993 *Nucl. Instrum. Methods* A **336** 1622
[84] Gemme G *et al* 1995 *J. Appl. Phys.* **77** 257–64
[85] Nigro A *et al* 1988 *Phys. Scr.* **38** 483–5
[86] Benvenuti C *et al* 1997 *Nucl. Instrum. Methods* B **124** 106–11
[87] Nigro A *et al* 1988 *Adv. Cryog. Eng.* **34** 813
[88] Di Leo R *et al* 1990 *J. Low Temp. Phys.* **78** 41–50
[89] Bosland P *et al* 1992 *Proc. EPAC 1992* p 1316
[90] Cantacuzène S *et al* 1994 *Proc. EPAC 1994* p 2076
[91] Marino M 1999 *PhD Dissertation* no 2039EPFL, Switzerland
[92] Marino M 1997 *Proc. 8th Workshop on RF Superconductivity* vol IV*(Abano Terme Padua, October 1997)* p 1076 133/98
[93] Sharma R G 2006 *Int. SRF Thin Films Workshop (LNL-INFN, Padova, Italy)* http://master.lnl.infn.it/thin lms/
Sharma R G 1987 *Cryogenics* **27** 361–78
[94] Stewart G R 2015 *Physica* C **514** 28–35
[95] Hardy G F and Hulm J K 1953 *Phys. Rev.* **87** 884
Hardy G F and Hulm J K 1954 *Phys. Rev.* **93** 1004
[96] Godeke A 2006 *Supercond. Sc. Technol.* **19** R68
[97] Müller G *et al* 1985 *Proc. 5th EPAC (London)* p 2085
[98] Peiniger M and Piel H 1985 *IEEE Trans. Nucl. Sc.* **32** 3610–2
[99] Perpeet M *et al* 1999 *IEEE Trans. Appl. Supercond.* **9** 2496–9
[100] Müller G *et al* 1997 *Proc. 5th EPAC (Sitges Barcelona, 10–14 June 1996)* ed S Myers *et al* (Bristol/Philadelphia: IOP Publishing) WEP002L 2085

[101] Posen S *et al* 2014 *Proc. IPAC 2014* WEPRI066 2641
Posen S and Lieppe M 2013 *Proc. 16th Int. Conf. on RF Superconductivity (Paris, France, September 2013)* TUP087 666
[102] Eremeev G *et al* 2013 *Proc. 16th Int. Conf. RF Superconductivity (Paris, France)* TUP071 603
[103] Becker C *et al* 2015 *Appl. Phys. Lett.* **106** 082602
[104] Posen S *et al* 2015 *Appl. Phys. Lett.* **106** 082601
[105] Posen S and Liepe M 2013 *Proc. PAC2013 (Pasadena, CA USA)* THOBA2 1091
[106] Deambrosis S *et al* 2006 *Physica* C **441** 108–13
[107] Franz S *et al* 2015 *Mater. Lett.* **161** 613–5
[108] Barzi E *et al* 2016 *Supercond. Sci. Technol.* **29** 015009
[109] Smith J F 1985 *Bull. Alloy Phase Diagr.* **6** 66–271
Smith J F 1989 *Phase Diagrams of Binary Vanadium Alloys* (Metals Park, Ohio: ASM International)
[110] Jorda J L and Muller J 1982 *J. Less Common Metals* **84** 39–48
[111] Andreone A *et al* 1995 *J. Appl. Phys.* **78** 1862
[112] Zhang Y, Palmieri V, Preciso R and Venturini W Reactive sputtered V_3Si films *Internal Note* LNL-INFN (REP) 144/99
Zhang Y 2000 Sputtering niobium films into a RFQ model & Sputtering of superconducting V3Si films, China Institute of Atomic Energy *PhD Dissertation* (http://www.surfacetreatments.it/upload/documentazione/86/3_Tesi%20PhD_Zhang%20Yan%20Completa.pdf)
[113] Zhang Y, Palmieri V, Preciso R and Venturini W Preliminary results on co-sputtering of V_3Si films by the facing-target magnetron technique *Internal Note* LNL-INFN (REP) 143/99
[114] Zhang Y *et al* Thermal diffusion of V3Si films LNL-INFN (REP) 157/2000
[115] Deambrosis S 2008 6 GHz cavities: a method to test A15 intermetallic compounds RF properties *PhD Dissertation* Padova, Italy
[116] Talvacchio J, Janocko M A and Greggi J 1986 *J. Low Temp. Phys.* **64** 395
[117] Gavaler J R *et al* 1974 in *Low Temperature Physics-LT-13, Vol. 3: Superconductivity, (Proc. 13th Int. Conf. Low Temperature Physics, Boulder, Colorado, 1972)* ed K D Timmerhaus *et al* (New York: Plenum Press) p 558
Gavaler J R, Janocko M A and Jones C K 1972 *Appl. Phys. Lett.* **21** 179–80
[118] Postnikov V S, Postnikov V V and Zheleznyi V S 1977 *Phys. Status Solidi* a **39** K21
[119] Andreone A *et al* 1989 *IEEE Trans. Magn.* **25** 1972
[120] Brewer L and Lamoreaux R H 1980 *At. Energy Rev.* **7** 195–356 Spec. Issue
[121] Valderrama E *et al* 2011 *Proc. 15th Int. Conf. on RF Superconductivity (Chicago, IL USA, 2011)* THPO077 930
[122] Nagamatsu J *et al* 2001 *Nature* **410** 63
[123] Buzea C and Yamashita T 2001 *Supercond. Sci. Technol.* **14** R115
[124] Floris A *et al* 2007 *Physica* C **456** 45–53
[125] Choi H J *et al* 2002 *Nature* **418** 758–60
[126] Liu Z K *et al* 2001 *Appl. Phys. Lett.* **78** 3678–80
[127] Xi X X *et al* 2007 *Physica* C **456** 22–37
[128] Xi X X 2009 *Supercond. Sci. Technol.* **22** 043001
[129] Xi X X 2014 private communication
[130] Xiao B P *et al* 2012 *Supercond. Sci. Technol.* **25** 095006
[131] Wolak M A *et al* 2014 *Phys. Rev. Spec. Top. Accel. Beams* **17** 012001
[132] Moeckly B H *et al* 2005 *IEEE Trans. Appl. Supercond.* **15** 3308
[133] Tajima T *et al* 2005 *Proc. PAC 2005* p 4215
[134] Oates D E, Agassi Y D and Moeckly B H 2010 *Supercond. Sci. Technol.* **23** 034011
[135] Vaglio R *et al* 2001 *Supercond. Sci. Technol.* **15** 1236
[136] Xi X X 2014 *6th Int. Workshop on Thin Films and New Ideas for Pushing the Limits of RF Superconductivity* (http://www.slideshare.net/thinfilmsworkshop/xiaoxing-xi-progress-in-the-investigation-of-mg-b2-thin-films-for-srf-cavity-applications)
[137] Takahashi H *et al* 2008 *Nature* **453** 376–8
[138] Putti M *et al* 2010 *Supercond. Sci. Technol.* **23** 034003
[139] Mizuguchi Y *et al* 2010 *Supercond. Sci. Technol.* **23** 054013
[140] Chen X *et al* 2014 Iron-based high transition temperature superconductors *Natl Sci. Rev.* **1** 371–95
[141] Kawaguchi T *et al* 2011 *Physica* C **471** 1174–6
[142] Lee S *et al* 2013 *Nat. Mater.* **12** 392–6
[143] Ueda S *et al* 2011 *Physica* C **471** 1167–73
[144] Kidszun M *et al* 2010 *Europhys. Lett.* **90** 57005
[145] Haindl S *et al* 2010 *Phys. Rev. Lett.* **104** 077001
[146] Haindl S *et al* 2013 *Int. J. Mod. Phys.* B **27** 1330001
[147] Gurevich A 2015 *AIP Adv.* **5** 017112
[148] Kubo T *et al* 2014 *Appl. Phys. Lett.* **104** 032603
[149] Kubo T 2015 *Prog. Theor. Exp. Phys.* **2015** 063G01
[150] Aurino M *et al* 2005 *J. Appl. Phys.* **98** 123901
[151] Antoine C Z *et al* 2010 *Phys. Rev. Spec. Top. Accel. Beams* **13** 121001
[152] Antoine C Z 2011 *IEEE Trans. Appl. Supercond.* **21** 3
[153] Roach W M *et al* 2013 *IEEE Trans. Appl. Supercond.* **23** 86002
[154] Antoine C Z, Villegier J- C and Martinet G 2013 *Appl. Phys. Lett.* **102** 102603
[155] Shiino T *et al* 2010 *Supercond. Sci. Technol.* **23** 045004
[156] Valente-Feliciano A-M 2015 *Proc. 17th Int. Conf. on RF Superconductivity (Whistler, BC, Canada, 13–18 September)* TUBA08 516
[157] Beringer D B *et al* 2013 *IEEE Trans. Appl. Supercond.* **23** 7500604
[158] Tan T *et al* 2015 *Appl. Phys. Lett. Mater.* **3** 041101